The Pennsylvania State University

The Graduate School

Department of Electrical Engineering

# MEASUREMENT AND ANALYSIS OF ATMOSPHERIC SPECIES USING A LOW POWER SUPERCONTINUUM LASER

A Thesis in

Electrical Engineering

by

Perry S. Edwards



Submitted in Partial Fulfillment
of the Requirements
for the Degree of

Master of Science

August 2009

The thesis of Perry S. Edwards was reviewed and approved* by the following:

C. Russell Philbrick
Professor of Electrical Engineering
Thesis Advisor

Zhiwen Liu
Associate Professor of Electrical Engineering

W. Kenneth Jenkins
Professor of Electrical Engineering
Head of the Department of Electrical Engineering

*Signatures are on file in the Graduate School

## ABSTRACT

Optical remote sensing systems operating on the principle of differential absorption have been employed since the mid-1970s for measuring airborne species. Multiwavelength sensing approaches, such as differential absorption lidar (DIAL) and differential absorption and scattering (DAS), are used for single (or a few) species detection boasting high sensitivity and long path detection capability. Broadband techniques, such as differential optical absorption spectroscopy (DOAS), are capable of detecting several species simultaneously over shorter path lengths and employ inversion algorithms to determine individual concentrations of the detected species.

This thesis presents an extension of earlier research using supercontinuum absorption spectroscopy (SAS) to measure atmospheric species. SAS is a broadband differential absorption approach that combines several of the best aspects of traditional multiwavelength, broadband, and hyperspectral techniques for atmospheric sensing. The key component of the SAS approach is a supercontinuum laser, which provides broadband capability while maintaining the qualities of a typical discrete wavelength laser source. This work presents measurements of atmospheric species acquired from a modified transceiver configured to operate on paths of 1 km range. Near-infrared spectra obtained using a high-resolution CCD grating spectrometer as a SAS detector compare well with MODTRAN$^{TM}$ simulations, and measurements of oxygen and water vapor absorption are used to demonstrate the capability and illustrate the potential for the SAS technique. A previously developed multiwavelength inversion algorithm is applied to the measurements to accurately determine the concentrations of oxygen and water

vapor while in the presence of other interfering species. The results presented validate the usefulness of SAS over long paths, and serve as a demonstration of SAS for near-infrared sensing of atmospheric trace species.

# TABLE OF CONTENTS

**LIST OF FIGURES** ..... **vii**

**LIST OF TABLES** ..... **x**

**ACKNOWLEDGEMENTS** ..... **xi**

**Chapter 1 Introduction** ..... **1**

**Chapter 2 Observations of Atmospheric Species** ..... **6**

2.1 Composition of the Atmosphere ..... 7
2.2 Natural and Anthropogenic Modifications to Composition ..... 8
2.3 Atmospheric Trace Species and Contaminants ..... 11
2.3.1 Naturally Occurring Trace Species ..... 12
2.3.2 Pollution Contaminants ..... 12
2.3.3 Aerosols ..... 13
2.4 Radiation Interaction with Atmospheric Species ..... 13
2.4.1 Scattering Processes ..... 13
2.4.2 Absorption Processes ..... 14
2.5 Summary ..... 16

**Chapter 3 Techniques for Absorption Measurements of Trace Species** ..... **17**

3.1 The Differential Absorption Measurement Technique ..... 18
3.1.1 A Generalized Approach for Differential Absorption Measurements ..... 18
3.1.2 Selection of a Differential Absorption Wavelength Pair ..... 23
3.1.3 Comparison of Techniques and Sources of Error ..... 26
3.2 Broadband Absorption Measurement Techniques ..... 27
3.2.1 Supercontinuum Absorption Spectroscopy (SAS) ..... 29
3.2.2 Comparison of Techniques and Sources of Error ..... 31
3.3 Summary ..... 33

**Chapter 4 SAS Experimental Configuration and Hardware** ..... **34**

4.1 Configuration of the Transceiver System ..... 34
4.2 Configuration of the Supercontinuum Source ..... 38
4.2.1 Spectral Bandwidth ..... 39
4.3 Alignment of the SAS System ..... 41
4.3.1 Components for Alignment ..... 41
4.3.2 Transmission Path and Retroreflector Placement ..... 42

4.3.3 Method for Beam Alignment....44
4.4 System Performance and Efficiency Estimations....46
4.4.1 Long Path Supercontinuum Beam Propagation....47
4.4.2 Fiber Coupling of Source and Detector....51
4.4.3 Modal Noise in Coupling Fibers....51
4.4.4 Summary of Total System Losses....53
4.5 Summary....54

**Chapter 5 SAS Long Path Measurements of Atmosphere Species....55**

5.1 SAS Analysis Techniques....55
5.1.1 Data Analysis Procedure....56
5.1.2 Multiwavelength Algorithm....59
5.2 Measurements and Calculations for Species Concentrations....61
5.2.1 Long Path Water Vapor Measurement....62
5.2.2 Long Path Oxygen Measurement....67
5.3 Summary....71

**Chapter 6 Summary, Conclusions and Future Work....72**

6.1 Summary....72
6.2 Conclusions....73
6.3 Future Work....74

**References....76**

# LIST OF FIGURES

Figure **2-1**: Observations of $CO_2$ concentration levels at Mauna Loa Observatory, Hawaii. Data up to 2003 is reported by the Climate Monitoring Diagnostics Laboratory of NOAA/ESRL and data from 2004-2009 is preliminary. ..... 9

Figure **2-2**: Results from analysis of techniques for measuring several greenhouse gases over the last 2000 years [IPCC-AR4, 2007]. ..... 11

Figure **3-1**: A spectral intensity plot demonstrating selection of a differential absorption wavelength pair. ..... 19

Figure **3-2**: A typical configuration for absorption measurements indicating the various processes that affect atmospheric path measurements (exaggerated for emphasis). ..... 21

Figure **3-3**: MODTRAN$^{TM}$ 5 atmospheric transmission simulation in the mid-IR region of 4.5 – 4.6 μm showing absorption bands for various trace species; the highlighted region is expanded in Figure 3-4. ..... 24

Figure **3-4**: MODTRAN$^{TM}$ 5 atmospheric transmission simulation in the mid-IR region of 4.555 – 4.569 μm show good choices of absorption lines for differential absorption measurements of $N_2O$. ..... 25

Figure **3-5**: Absorption spectra for many atmospheric species in the UV and visible. The widely varying structures allow for simple identification of each species [Figure from: Platt and Stutz, 2008]. ..... 28

Figure **3-6**: The seeding of the signal and idler frequencies during the four-wave mixing process are shown at low pump powers in a PCF; at high pump powers the process has cascaded to provide a wide band spectral output (color bar values are in units of dBm) [Figure from: Wadsworth *et al.*, 2004] .... 31

Figure **4-1**: Configuration of the transceiver system located in the rooftop laboratory of the Electrical Engineering East building on the Penn State campus. Optical elements M-x are mirrors, OBL-x are objective lenses, and L-1 is a biconvex lens. M-5 is a corner cube retroreflector located on a distant rooftop completing the 890 m folded path. Mirrors M-6 and M-7 form a Newtonian telescope configuration. ..... 35

Figure **4-2**: Picture of the rooftop transceiver system with the outgoing path highlighted. ..... 36

Figure **4-3**: Configuration of the supercontinuum source. The PCF is coiled in the Blaze Photonics packaging for protection. ..... 39

Figure **4-4**: (a) Measured supercontinuum power spread at the PCF fiber exit after a neutral density filter in dBm [Brown *et al.*, 2008b] and, (b) measured supercontinuum output after 25 m of SMF-28 fiber. ..... 40

Figure **4-5**: The Supercontinuum output power at the exit aperture of the rooftop end of the SMF-28 fiber, in nW/nm. ..... 40

Figure **4-6**: A 3-D pictorial shows the rooftop transceiver arrangement located on the Electrical Engineering East building on the Penn State campus. ..... 41

Figure **4-7**: Path configurations across the Penn State campus and downtown region of State College, PA. ..... 43

Figure **4-8**: (a) View of the location of the corner cube retroreflector as seen from behind the turning mirror (M-4 in Figure 4-1) located on the rooftop of the Electrical Engineering East building on the Penn State campus. (b) A view of the retroreflector through the 10" telescope during early morning hours towards the end of a night of measurements. ..... 44

Figure **4-9**: Simuations for intensity distribution of a gaussian beam 890 m down range per wavelength (0.35 – 1.75 μm) for (a) 1.0 cm initial output beam and (b) 1.5 cm output beam. ..... 49

Figure **4-10**: Simulated beam spread for propagation of a Gaussian beam at 890 m down range for a 1.0 cm initial output beam and a 1.5 cm beam. ..... 50

Figure **5-1**: Reference spectra fits (20 point and 120 point) used in the analysis algorithm, which is applied to the raw experimental data, are plotted for the spectral region of an oxygen absorption feature. ..... 57

Figure **5-2**: Several water vapor absorption measurements superimposed demonstrating repeatability and the dotted line represents the reference spectrum fit used in the analysis procedure. ..... 59

Figure **5-3**: MODTRAN$^{TM}$ 5 transmittance simulation for the atmospheric constituents present within the spectral bandwidth of the supercontinuum source. ..... 61

Figure **5-4**: The measured absorption spectra for atmospheric water vapor transmittance at 1 $cm^{-1}$ resolution over the 890 m path are compared with a MODTRAN™ 5 simulation. ..... 64

Figure **5-5**: (a) HITRAN line calculations broadened for temperature and pressure are convolved with the slit width of 6.4 $cm^{-1}$ to compare to the high resolution measurement from Figure 5-4. (b) MLE algorithm inversion result for estimation of water vapor concentration. ..... 65

Figure **5-6**: Measurements of relative humidity and temperature recorded a MET station located 5 m from the measured path at the time of SAS water vapor measurements indicated. ..... 66

Figure **5-7**: MODTRAN™ 5 Simulated transmittance spectra showing an oxygen absorption band and a long path absorption measurement for the same region superimposed for comparison. ..... 68

Figure **5-8**: (a) HITRAN line calculations (blue line) broadened for temperature and pressure, then convolved with the slit width of 6.4 $cm^{-1}$ compared with the high resolution measurement for oxygen shown in Figure 5-7 (red line). (b) MLE inversion algorithm result for atmospheric oxygen demonstrating quick convergence on the concentration value. ..... 70

Figure **5-9**: MLE algorithm inversion convergence calculation for atmospheric oxygen using 400 wavelengths in the 750 to 775 nm region. A 20 point average of the resulting is also shown (red line). ..... 71

# LIST OF TABLES

Table **2-1**: Main components of the dry atmosphere and their mixing ratios [USSA76, 1976]. ..... 7

Table **3-1**: Comparison of DOAS and SAS sources. ..... 32

Table **4-1**: Optical components used in the transceiver portion of the SAS system are identified with components shown in Figure 4-1. ..... 37

Table **4-2**: Estimated power efficencies for the SAS system. Several of the components optical efficiencies are reported from their respective datasheets, estimations based on typical incident and reflected/refracted power measurements, or calculated**.** ..... 53

# ACKNOWLEDGEMENTS

This thesis only describes the scholarly and experimental results of my research. It does not provide any indication of the level of support I received from others: my advisors, peers, friends, and family. To that point, here I acknowledge and thank those who contributed their time and effort to assisting me in completing this work.

First and foremost, I thank Dr. Philbrick for his guidance and support during times of research and his thorough reviews during my documentation efforts. A devotion to becoming a "curious observer", the assertion of "Don't ever give up", along with several other customs and ideas I learned from Dr. Philbrick – I thank him for it all.

Next, I must thank Dr. Zhiwen Liu for his guidance and support as well as equipment support. I greatly appreciated his useful suggestions and assistance when I was confounded by the occasional experimental predicament.

I also thank the students and researchers in the Ultrafast Optics lab: Kebin Shi, Haifeng Li, Qian Xu, Chuan Yang, Yifan Huang, and visiting scholar Zhe Zhang. In particular, Kebin, Haifeng and Qian for their lab support and Zhe for his experiment support.

Additionally, for countless hours of experiment support, I thank Nicole Sherman, Vladimir Getman and my fellow Lidar lab member Andrea Wyant. Without their assistance during several long, cold winter nights of running experiments there would be few quality results to show in this work.

I must acknowledge the previous research and papers related to this work, which are referenced in this thesis, and those who headed the initial efforts: Joe Begnoché and Dave Brown. Dave, thank you for all your guidance, assistance, and support as well as your previously developed work. Your efforts provided an excellent foundation to build upon.

Finally, I must give a special thanks to my parents for always believing in me and supporting me as I continue to strive towards achieving my goals.

**Chapter 1**

# Introduction

The unrelenting quest to better monitor, model, and thus predict the anthropogenic emission influences on meteorological process and climate change continues to promote the development of several atmospheric remote sensing technologies. In particular, sensing systems capable of detection and quantification of atmospheric species are of primary interest. This is due to the concerns about increasing concentrations of certain chemical species, and their importance in controlling several environmental factors that affect global warming, stratospheric ozone depletion, and formation of photochemical smog. Increasing concentrations of chemical species resulting from human activity are major contributors to global climate change.

There are three primary methods for measuring atmospheric species. The first method, involves extraction of an atmospheric sample into a portable container or a filter surface, or suspended in a solution for later analysis by a laboratory instrument. This method provides a simplistic approach but each sample is limited to one point in space at one time and is often impractical for implementation for investigations of atmospheric processes. Also, the gas or particulate is removed from its environment and thus is influenced by the containers, the surface, or the suspension environment. The second approach, similar to the first, consists of bringing a ruggedized or simplified laboratory instrument into the outdoor environment. These techniques are referred to as *in-situ* sensing, and inherently have an advantage in providing real-time measurements, but often

with a reduced accuracy, selectivity, and sensitivity compared to that achieved using extracted samples analyzed within a laboratory environment. *In-situ* measurements may be ground-based, or they may be implemented via weather balloons, sounding rockets, or aircraft outfitted with instruments capable of analyzing the composition of atmospheric gases. The useful range of spatial and temporal information gathered depends upon locating and operating a point measuring sensor in time and space dimensions. Typical instruments used for *in-situ* measurements include mass spectrometers, photo-spectrometers, particle counters, scatterometers, and absorption spectrometers. The third method for atmospheric species sensing involves remote sensing techniques. Remote sensing instruments record observations of the scattering or absorption of acoustical and electromagnetic radiation source interaction with the atmosphere to detect a physical property of the atmospheric medium based upon this interaction using an instrument located at a distance. This technique has similar advantages to *in-situ* detection, such as real-time measurement; additionally, it has the advantage of being able to collect data continuously over some extended range of time and space. The useful range of remote sensors may be limited by interference from other atmospheric effects, such as unwanted scattering or turbulence along the measurement path. For the purpose of atmospheric sensing of chemical species, optical remote sensing techniques provide the greatest capability. By exploiting the physical interaction of light with molecules and remotely monitoring the interaction processes (absorption or scattering), sensors can detect chemical species and measure their concentrations.

Several optical remote sensing methods have been developed for atmospheric measurement applications. The types of optical sensing generally fall into two broad

categories, which are commonly referred to as techniques involving active or passive sensing. Active remote sensing transmits an electromagnetic or acoustical signal to probe a gaseous region, whereas the passive techniques generally use solar radiation or ambient light as their source. Measurements of scattering, absorption, fluorescence, and several other interaction phenomena provide information useful to detect species, measure concentrations, or determine physical properties of the medium for the gas under study. Lasers provide an important transmitter source used today for accomplishing many of these types of measurements. Lasers provide high spatial and temporal coherence properties which allow longer path measurements. The selection of an operating wavelength is based on the desired type of measurement. Laser remote sensing systems are used over horizontal or vertical paths configured for ranging, referred to as light detection and ranging, or lidar. In a lidar configuration the location of the target volume is determined by a time delay in the returns of a pulsed signal from a scattering volume. Alternatively, another laser remote sensing technique uses the integrated path approach, where the concentration of a species is determined by absorption over the total path length.

Recent experiments implemented in the Penn State Lidar Laboratory utilize a broadband supercontinuum laser source on a horizontal path to measure integrated path absorption of atmospheric species [Edwards *et al.*, 2009; Brown *et al.*, 2008a and 2008b]. Broadband laser sources provide several advantages over traditional laser sources for these absorption measurements, as described in Chapter 3 of this work. A supercontinuum broadband laser source typically provides emission in the visible and near infrared that is essentially continuous over wavelength intervals of several hundred

nanometers. When used to probe the atmosphere, absorption features of multiple atmospheric species, together with any overlapping interferents, are observed simultaneously as the signal is recorded by an imaging detector of a high-resolution spectrometer or optical spectrum analyzer. This technique offers a unique approach for atmospheric sensing that combines several of the best features of the traditional methods. Earlier methods included multiple wavelength systems, such as two or three wavelength Differential Absorption Lidar (DIAL) [Murdock *et al*., 2008], as well as broadband Differential Optical Absorption Spectroscopy (DOAS) [Platt, 2004; Platt and Stutz, 2008] and hyper-spectral systems [Stothard *et al.*, 2004] for studies of atmospheric constituents.

This thesis presents an extension of earlier research to improve detection and measurement of atmospheric trace species using the techniques of supercontinuum absorption spectroscopy (SAS). The SAS system at Penn State University has undergone a series of development efforts to improve the capability for measuring atmospheric species. Initial proof of concept studies were conducted within a laboratory environment using a folded path to make measurements of indoor humidity, and demonstrated that the technique correlated well with *in-situ* measuring devices [Begnoché, 2005; Brown, 2008]. The next phase of SAS development relocated the transmitting and receiving system to a small roof-top laboratory and used a supercontinuum laser for open-path atmospheric measurements. Horizontal atmospheric paths of 150 m and 300 m across the Penn State campus successfully demonstrated measurements of water vapor for a range of atmospheric conditions that compared well with local MET station humidity measurements. Further studies demonstrated the capability of measuring the atmospheric

oxygen density along the path with a precision and accuracy of better than five significant figures [Brown *et al.*, 2008a and 2008b; Edwards *et al.*, 2009].

The present SAS system at Penn State has been improved over the previous versions and now operates over horizontal path lengths approaching 1 km [Edwards *et al.*, 2009]. The configuration reported here actually operates on an 890 m path across the campus and downtown State College area. Previous configurations operated over approximate paths of 150, 300, 540 m across the Penn State University campus. The advantage for utilizing the longer path is twofold. The extended path length provides the opportunity to test the SAS system over longer ranges permitting lower species concentrations and added atmospheric effects, such as turbulence and scattering, to be studied. Also, the longer path is more useful for real world applications for pollution monitoring, where longer path integrated absorption allows measurements of lower concentration of trace species. This capability leads to greater sensitivity for detecting of atmospheric species that exist at lower background absorption levels, and effectively increases the signal to noise (SNR) to allow improved accuracy for concentration measurements.

## Chapter 2

# Observations of Atmospheric Species

The Earth's atmosphere is subjected to a variety of phenomena that affect its' composition and structure. Historical records and geological studies compared with modern day observations of the atmosphere indicate that the atmosphere has been significantly altered by solar and terrestrial processes. During the past two centuries, the industrial revolution has caused a dramatic increase in anthropogenic emissions from human activity that has modified the Earth's atmosphere. Besides direct observation of changes in species concentrations, evidence is also provided through observations of environmental and climatic changes observed as the greenhouse gas warming effect, stratospheric ozone depletion, and elevated photochemical smog levels [IPCC, 2007]. Studies of recent climatic changes show that the Earth has entered a period of global warming that is being brought on by a human disturbance, rather than through natural cycles of the Earth that are indicated in geological records. Increasing levels of greenhouse gases and other harmful trace species are detected with obvious sources possessing the optical "fingerprints" of human activity [IPCC, 2007]. This chapter discusses the composition of the atmosphere including an introduction to harmful trace species. The processes involved in optical detection and measurement of atmospheric species are discussed; thereby leading to a discussion of optical detection methods in Chapter 3.

## 2.1 Composition of the Atmosphere

The composition of the Earth's atmosphere is in a constant state of flux. Transport processes shuttle atmospheric constituents over local and global scales as well as mix them over vertical distances. The main components of the atmosphere are therefore well mixed through the troposphere, stratosphere, and mesosphere up to the height of the turbopause near 95 km. The average mixing ratios for the main constituents in the dry atmosphere are provided in Table 2-1. The top three components of the atmosphere (nitrogen, oxygen, and argon) constitute nearly 99.9% of the dry atmosphere. The other 0.1% contains all additional species, which are deemed to be minor constituents or trace species of the atmosphere [USSA76, 1976]. All of the trace species are present in levels less than 1000 parts per million by volume, with the exception of water vapor, which is present in a significant abundance in the troposphere, typically between 0.001% and 1%, but can be as much as 3%. Its' changes in physical state as a

Table **2-1**: Main components of the dry atmosphere and their mixing ratios [USSA76, 1976].

| Gas | Chemical formula | Mixing ratio by volume (%) |
|---|---|---|
| Nitrogen | $N_2$ | 78.08 |
| Oxygen | $O_2$ | 20.95 |
| Argon | Ar | 0.93 |
| Carbon dioxide | $CO_2$ | 0.037 |
| Neon | Ne | 0.0018 |
| Helium | He | 0.00052 |
| Methane | $CH_4$ | 0.00017 |
| Krypton | Kr | 0.00011 |
| Xenon | Xe | 0.00009 |
| Hydrogen | $H_2$ | 0.00005 |
| Dinitrogen oxide | $N_2O$ | 0.00003 |

function of temperature and pressure causes water vapor to be the primary factor in transport of heat energy from the equatorial to polar regions. The concentration of water vapor modifies the mixing ratios of the various atmospheric constituents in the total density, and it is considered to be a major constituent of the wet tropical atmosphere.

## 2.2 Natural and Anthropogenic Modifications to Composition

Urbanization, factory pollution, combustion byproducts, and several other sources of pollutants modify the atmosphere's chemical composition. Several U.S. and international climate study organizations site these sources and their affects on the environment (i.e. the U.S. Environmental Protection Agency (EPA), NASA, and Intergovernmental Panel on Climate Change [IPCC-AR4, 2007]). The primary pollution and greenhouse gas components emitted from the various sources are categorized by their base molecule and are separated into groupings; nitrogen, sulfur, and carbon containing species. Sulfur based species tend to assist in the nucleation development of aerosols, which contribute a net cooling effect by increasing the planetary albedo through cloud formation. Other greenhouse gases such as carbon dioxide ($CO_2$), methane ($CH_4$), nitrous oxide ($N_2O$), and many of the chlorofluorocarbons (CFCs, HCFCs), are primary carbon and nitrogen based species that generally contribute to warming of the Earth's atmosphere by reducing the window of IR emission back into space, i.e. the greenhouse gases. Several additional species contribute to warming and cooling of the Earth as well as the other climatic events mentioned previously (i.e. carbon

monoxide contributes to development of photochemical smog; isoprene and terpenes are highly reactive and participate in the formation of ozone).

Evidence of change in atmospheric composition is best observed through long-term studies of atmospheric species. A long-term monitoring study of monthly atmospheric $CO_2$ observations at Mauna Loa Observatory, Hawaii demonstrates a steady increase over the last 50 years in $CO_2$ concentration. The monthly observations are plotted in Figure 2-1. Since 1958, $CO_2$ levels have risen by more than 70 ppm (~22%). This notable increase is quite significant when compared to the global background average of $CO_2$ of 280 ppm during the preindustrial era [IPCC-AR4, 2007].

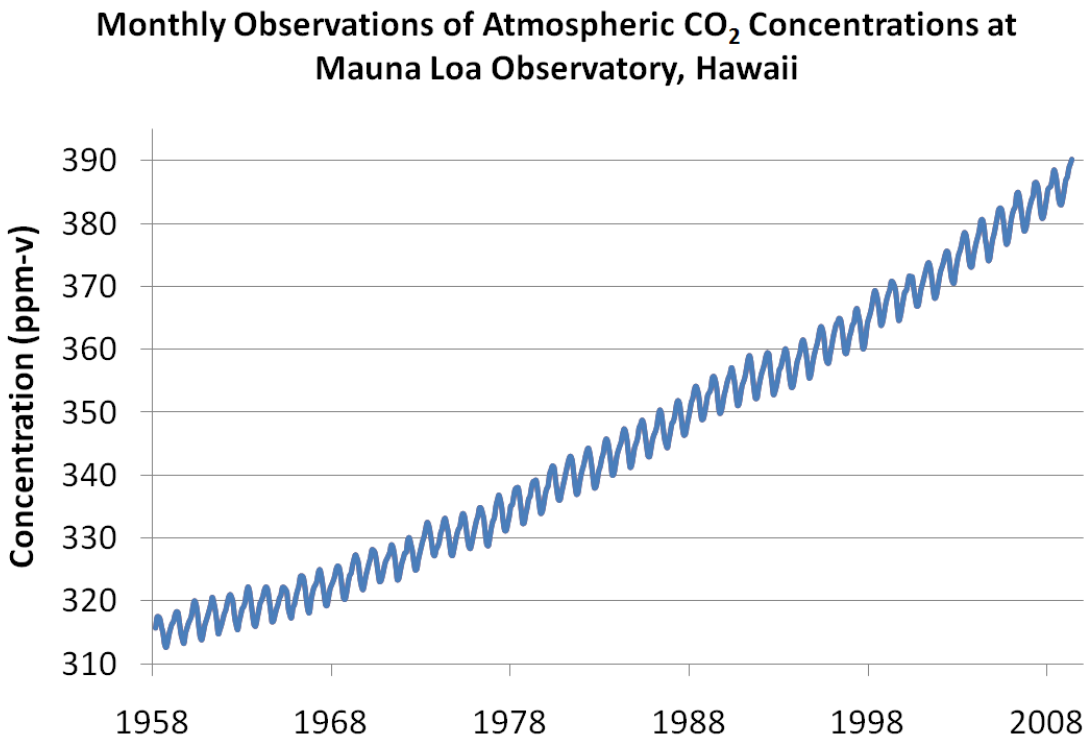


Figure **2-1**: Observations of $CO_2$ concentration levels at Mauna Loa Observatory, Hawaii. Data up to 2003 is reported by the Climate Monitoring Diagnostics Laboratory of NOAA/ESRL and data from 2004-2009 is preliminary.

Model predictions estimate that background $CO_2$ levels will eclipse 500 ppm by 2050, based upon the current rate of manmade greenhouse gas production, [IPCC-AR4, 2007]. It is generally agreed in the scientific community that once 450 ppm $CO_2$ levels are reached, irreversible damage to the Earth's climatology will occur. It is interesting to note that the summer growth of vegetation in the northern hemisphere causes a yearly minimum in the $CO_2$ as carbon is sequestered in plants by photosynthesis. The $CO_2$ added by winter heating and burning fossil fuel quickly contributes to the increase, along with the background sources from power generation and transportation.

In the 4$^{th}$ IPCC assessment of global climate change, greenhouse gases are classified based off their ability to impact the environment. Each species exhibits a radiative efficiency (in W-m$^{-2}$-ppb$^{-1}$) that defines their potential to cause an impact, which is described as the energy flux change of Earth's infrared radiation per unit surface area of the globe at the top of the atmosphere. This rate of change is referred to as radiative forcing defined in W-m$^{-2}$, with a positive net change signifying a warming in the atmosphere. Calculations in the IPCC assessment show that $CO_2$ levels in 2005 contribute 1.66 W-m$^{-2}$, and other significant contributors include, $CH_4$ at +0.48 W-m$^{-2}$, and $N_2O$ at +0.16 W-m$^{-2}$. When compared to 1995 contributions for $CO_2$ (1.38 W-m$^{-2}$), we find that an increase of nearly 20% has occurred. Figure 2-2 shows the increases in concentrations of the three primary contributors to radiative forcing during the last 2000 years. The figure emphasizes the drastic increase in concentration of these gases since the industrial revolution era began (approximately 1750).

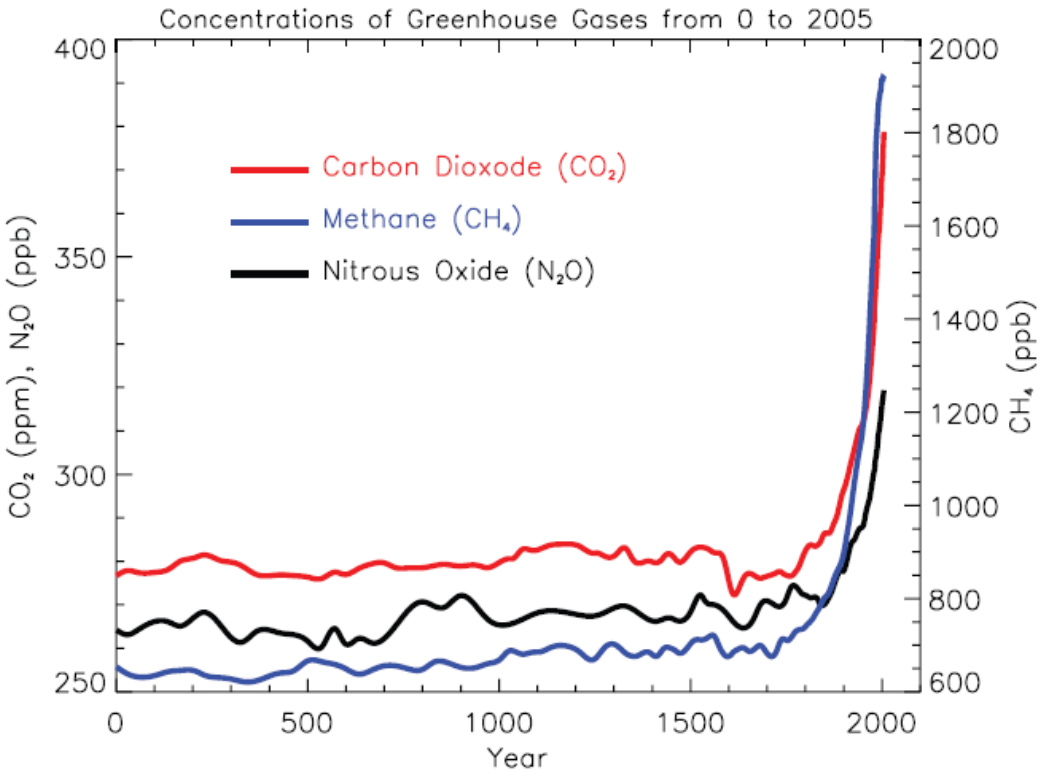


Figure **2-2**: Results from analysis of techniques for measuring several greenhouse gases over the last 2000 years [IPCC-AR4, 2007].

## 2.3 Atmospheric Trace Species and Contaminants

Trace species constitute less than a tenth of one-percent of the Earth's gaseous atmosphere. Despite their miniscule contribution in volume, they possess great significance in the chemical and radiative processes in the atmosphere. Stratospheric ozone filters UV radiation from the sun that proves deadly to organic life. Ammonia ($NH_3$) acts as a neutralizer for various acidic compounds. Nitrogen oxides ($NO_x$) regulate many trace species cycles and influence the degradation of several other species [Geyer *et al.*, 2001; Stutz *et al.*, 2004]. These examples represent only a small fraction of the total influence trace species have on the atmosphere. Several trace species and their

interactions with the atmosphere are naturally occurring, while others originate from human activity. This is briefly discussed in the following sections.

### 2.3.1 Naturally Occurring Trace Species

The majority of trace constituents exist in the atmosphere due to chemical processes that occur in nature. Several species result from the organic breakdown of vegetation and emissions from biomass, these include methane, nitrogen compounds, and carbon monoxide. Additional contributions result from natural sources of trace species, including volcanic emissions (sulfur dioxide, carbon dioxide, and others) and lightning (nitrous oxide). In geological records, naturally occurring processes (besides a volcanic or other spontaneous event) tend to follow cyclical climate trends, and these have been the subject of many scientific studies that provide tools for prediction using climate models for forecasting.

### 2.3.2 Pollution Contaminants

The sources of trace species that are categorized as pollution are most often produced through human activity. Many of these same species already occur naturally in the atmosphere; however, pollution causes them to exist at elevated concentration levels caused by human activity. Obvious sources of air pollution include fossil fuel burning at power generation plants and factories (carbon dioxide, sulfur dioxide), automobile

combustion exhaust (carbon monoxide, nitrogen oxide/dioxide), and agriculture production (methane, nitrogen compounds, carbon monoxide/dioxide).

### 2.3.3 Aerosols

Atmospheric aerosols primarily occur naturally from water vapor condensation on nuclei to form clouds and fog, and only about 10% of the aerosol occurrences have anthropogenic origins. In addition to water vapor sources, aerosols are formed by nucleation on suspended dust particulates, biogenic materials, and photochemical smog. The lifetime duration that an aerosol will remain suspended is related to the size of the aerosol, and the physical properties of the suspension medium. Settling velocity, which varies with the square of the particle radius, defines the upper limit on aerosol size of around 10 μm. Large aerosols, such as road side dust, settle quickly and have very short residual suspension times in air. Smaller aerosol sizes are defined by the differentiation between molecules and aerosols near 1 nm in radii.

## 2.4 Radiation Interaction with Atmospheric Species

### 2.4.1 Scattering Processes

Aerosol and particulate scattering affects and limits the propagation of light through the atmosphere. The scatterers exist over a range of diameters, and are often non-uniform in shape and size. The non-uniformities create several complexities in analysis of the scattering from these particles because the scattering solutions become

complicated. However, by making the approximation of a spherical scatterer, the scattering solution is simplified and provides a good approximation for describing the scattering processes in the atmosphere. The method for calculating the spherical scatter approximation was presented by Mie (1908). His analysis of the scattering from dielectric spheres of varying diameters provided a detailed solution for radiation scattering. Mie scattering generally refers to scattering by particles much larger than the wavelength of incident light. Raleigh scattering [Young, 1981], which can also be described by the small scale limit of the Mie solution, describes the elastic scattering of radiation by particles whose size is very small compared to the wavelength of incident light. The Raleigh scattering coefficient used in the scattering solution, is obtained by multiplication of the Rayleigh scattering cross section and air density, and it is proportional to $\lambda^{-4}$. The large scale limit of the Mie solution, where scatter diameters are greater than one hundred times the wavelength of radiation, can generally be described by ray trace theory.

### 2.4.2 Absorption Processes

Absorption, as well as scattering, can cause losses along an optical path in the atmosphere. Absorption of light may occur due to the electrons bound in atoms or molecules (electronic level excitation – UV and VIS) or due to vibrational, rotational, stretching, bending of the molecular bonds (molecular quantum excitation – infrared). Molecular absorption is the most easily observed property that uniquely identifies the quantum energy states of molecules at infrared wavelengths. The fundamental absorption

features lie in the infrared beyond 2.5 μm corresponding to the vibrational energy states of molecules. Absorption of electromagnetic radiation occurs in molecules when the quantum energy transition states correspond to the radiation's frequency. The energy is coupled into the molecule through oscillations of the molecule's dipole moment which cause the molecule to bend and stretch. Asymmetrical stretching creates an unbalanced oscillation of the dipole moment and excites vibrational modes at frequencies which correspond to infrared spectral features [Atkins, 1990]. Several types of molecules undergo strong line absorption throughout the infrared; the most noticeable being water vapor. The vibrational modes of water vapor are so strong in the infrared, that overtones of these modes are observed through the near-infrared and into the visible portions of the spectrum. Additional species exhibiting asymmetrical stretching also produce infrared absorption spectra that are unique to each species chemical structure. The combination of vibrational modes and overtones of various species and the electronic states of molecules provide absorption features in the optical spectrum from the ultra-violet (UV) to infrared (IR) region.

The relative spectral widths of the absorption lines are determined by the lifetimes of the energy states, and depend on the natural lifetime modified by collision and Doppler motion from thermal motion. The lifetime of the molecule is therefore sensitive to temperature and pressure, which contribute to broadening of the natural width of the absorption lines. The molecular cross-section which corresponds to the lifetime of the species, multiplied by the concentration of the species, results in the absorption coefficient in which is used in describing the attenuation of radiation passing through a medium.

## 2.5 Summary

Clear evidence of global climate change due to anthropogenic influence is recognized today by the scientific community and gradually by governments throughout the world. Atmospheric sensors that operate on the various schemes for optical detection of molecular-radiation interaction continue to provide highly accurate measurements of atmospheric species. As the scientific community develops a better understanding of the complex processes involved with global climate change, strong motivation exists to develop more accurate, capable sensors for atmospheric sensing. Here we have described the background of that motivation and Chapter 3 presents a new technique (SAS) that promises improved measuring capability.

# Chapter 3

## Techniques for Absorption Measurements of Trace Species

Over the years several techniques have been developed for detection of chemical species that make use of the property of molecular absorption, as described in Chapter 2. The laboratory techniques in the field of spectroscopy are well developed. These use light absorption or scattering from molecular species to identify and quantify the species concentration. Absorption measurements are also conducted remotely using lidar techniques for atmospheric measurements. The short list of the possible laboratory and open path optical techniques includes Raman spectroscopy, Raman lidar, Differential Absorption Lidar (DIAL), Differential Absorption and Scattering (DAS), Differential Optical Absorption Spectroscopy (DOAS), Cavity-Ringdown Spectroscopy (CRDS), Cavity-Enhanced Absorption Spectroscopy (CEAS), External Cavity Quantum Cascade Laser Spectroscopy (EC-QCLS), Laser-Induced Fluorescence (LIF), and Tunable Diode Laser Spectroscopy (TDLS). For measurements along an open air path, the differential absorption and Raman scatter techniques have proven themselves to be reliable methods for detection and quantification; the absorption techniques serve as the focus for the work reported here.

## 3.1 The Differential Absorption Measurement Technique

Traditional DIAL and DAS approaches have been used for several decades, since the first implementation by Schotland [1965]. The techniques developed then have evolved to form the basis of the approaches used today, including both simple and advanced differential absorption systems. These techniques coupled with improvements in hardware provide instruments for detection and measurement of atmospheric absorption. The absorption measurements are inverted to calculate concentration values of the selected species and they can be used to measure gaseous species concentrations as low as the parts-per-trillion (ppt) range. The techniques used to implement various differential absorption measurements are discussed in this section.

### 3.1.1 A Generalized Approach for Differential Absorption Measurements

A generalized approach for performing a differential absorption measurement exists at the core of all DIAL and DAS systems. Implementing one of these systems requires a transceiver configuration that transmits and measures the backscatter signals at two (or more) optical wavelengths. A pair of wavelengths is typically chosen such that one wavelength is matched with an absorption feature of the selected gaseous species and the other is located slightly off the absorption features. This selection of "on" and "off" wavelengths constructs what is often referred to as a differential absorption pair, and is illustrated in Figure 3-1.

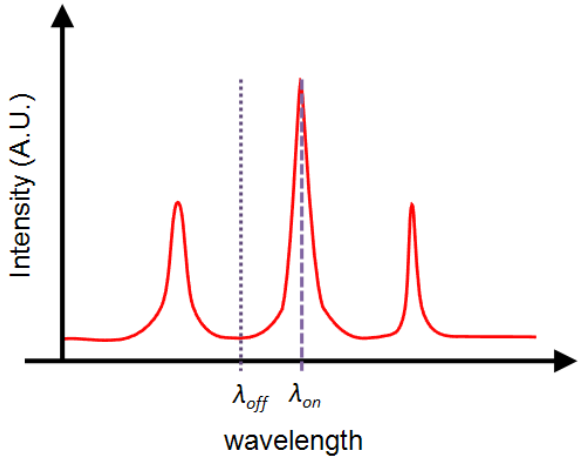


Figure **3-1**: A spectral intensity plot demonstrating selection of a differential absorption wavelength pair.

The light sources used in differential absorption systems are selected and configured to operate at the chosen on- and off-wavelengths. Analysis techniques used in traditional DIAL systems require that the on-wavelength light source exhibits a narrow linewidth comparable with the natural line width of the absorption feature exploited in the measurement. The most difficult part of DIAL measurement is matching the laser wavelength and line shape with that of the absorption feature to be measured, or in determining the spectral overlap function. The wavelength pair is selected to avoid spectral overlap of the sources operating at the two wavelengths in order to minimize distortion of the measurement, and the off-wavelength should also be located where no other species is absorbing. Laser sources are commonly used for differential absorption lidar systems because of the advantage of their narrow linewidths and high peak power. When configured with a pulsed (Q-switched) output beam, lasers provide the capability for obtaining range resolved measurements in the DIAL configuration. The second approach, DAS, uses a return from a hard target or retro-reflector, rather than the

atmospheric scatter from aerosols, and measures the path integrated absorption. A third approach uses a broad wavelength source and measures the scattered signals with a spectrometer. In this case all of the spectral selection is accomplished in the detector, and the differential absorption technique is referred to as broadband absorption spectroscopy or DOAS. This approach is discussed more thoroughly in section 3.2.

The DAS and DOAS techniques use light sources that transmit through an open air path containing the target trace species to be measured. Several of the scattering and absorption processes mentioned in Chapter 2 are typically encountered as the light travels along the path, and they usually reduce the spectral intensity at the end of the path. Open air propagation measurements may be further complicated when the atmosphere contains additional species, other than those targeted for the measurement; in particular, when those species have optical absorption features in the same spectral region as the target species. Figure 3-2 shows the typical configuration for DAS or DOAS systems and the various processes that affect the light intensity measured by the detector. The difference between the DAS and DOAS systems is somewhat overlapped in the literature, but the DAS instrument usually refers to a laser source using two or more wavelengths, and the DOAS usually refers to use of a broadband incoherent or discharge source as the transmitter.

Typical DIAL systems use the signals backscattered from volume elements along the path to detect and measure the range resolved concentration of the selected species. Alternatively, DAS systems often use hard targets over a fixed path length, and have the advantage of increased signal return, but at the expense of range resolution. The signal energies received by the detector at the on- and off-wavelengths are used with the

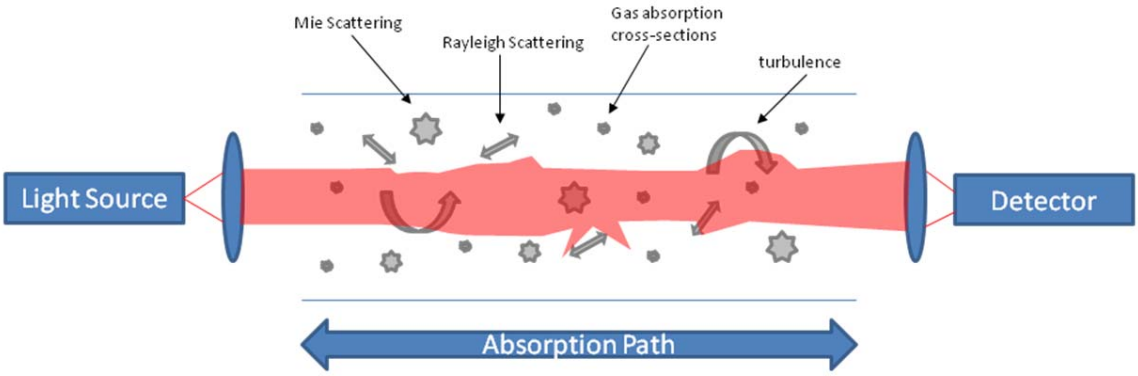


Figure **3-2**: A typical configuration for absorption measurements indicating the various processes that affect atmospheric path measurements (exaggerated for emphasis).

traditional lidar equation and information on the relationship between the laser line and species line shapes to analyze a differential absorption measurement [Measures, 1984]. The equations for the return energies at the "on" and "off" wavelengths are given as (formulated by Brown [2008]),

$$E_{rec,on}(\lambda_{on}, R_T) = E_{out,on} \frac{A}{{R_T}^2} \xi(\lambda_{on}) \xi(R_T) \frac{\rho^s \tau_d}{\pi \tau_L} e^{-2\int_0^{R_T} \left[\kappa(\lambda_{on},R)+N(R)\sigma^A(\lambda_{on})\right] dR} \quad [3.1]$$

$$E_{rec,off}(\lambda_{off}, R_T) = E_{out,off} \frac{A}{{R_T}^2} \xi(\lambda_{off}) \xi(R_T) \frac{\rho^s \tau_d}{\pi \tau_L} e^{-2\int_0^{R_T} \left[\kappa(\lambda_{off},R)+N(R)\sigma^A(\lambda_{off})\right] dR} \quad [3.2]$$

where,

$E_{out,on}$ , $E_{rec,on}$ are the respective energies transmitted and received per pulse at the online or measurement wavelength [J],

$E_{out,off}$ , $E_{rec,off}$ are the respective energies transmitted and received per pulse at the offline or reference wavelength [J],

$\xi(\lambda_{on})$ $\xi(\lambda_{off})$ are respectively the total optical efficiency at on and off wavelengths $\lambda_{on}$ and $\lambda_{off}$, for all optical elements [unit less],

$R_T$ is the range to the topographical scattering target [m],

$\xi(R_T)$ is the probability that radiation from range $R_T$ reaches the detector based on geometrical considerations,

$\tau_d$ is the detector integration period [s],

$\tau_L$ is the pulse duration period [s],

$\rho^s$ is the scattering efficiency of the target [unit less],

$N(R)$ is the number density of the absorbing species [# $m^{-3}$ ],

$\sigma^A(\lambda_{on})$, $\sigma^A(\lambda_{off})$ are the absorption cross sections [$m^2$] for the species of interest at the online and offline wavelengths $\lambda_{on}$ and $\lambda_{off}$,

$\kappa(\lambda_{on},R_T)$, $\kappa(\lambda_{off},R_T)$ are the attenuation coefficients of the atmosphere to the online and offline wavelengths $\lambda_{on}$ and $\lambda_{off}$ independent of the absorbing species [$m^{-1}$] and,

A is the area of the receiving telescope [$m^2$].

The results from the differential absorption technique are obtained by taking the ratios of the two return energies to provide the absorption measurement which follows the Lambert-Beer law. Also, by taking the ratio of the return energies, the $1/R^2$ dependence of the scattering geometry cancels out of the resulting equation. This ratio is combined with the measured cross-sections for the spectral features of interest and the information on the wavelength overlap functions of the laser and the spectral line of the absorbing species to calculate number density values for the species. Integrated path

measurements provide concentration-path-length (CPL) values when using typical DAS technique with a hard target configuration by using the relation,

$$CPL = \int_0^{R_T} N(R)dR = \frac{R_T}{2\sigma_{diff}^A}\left(\ln\left[\frac{E_{rec,off}(\lambda_{off}, R_T)}{E_{rec,on}(\lambda_{on}, R_T)}\right]\right), \qquad [3.3]$$

where $\sigma_{diff}^A$ is the differential cross section for the on- and off- wavelengths. CPL values are often reported instead of mixing ratios for trace species concentration measurements due to their existence as small factions per volume of the total atmospheric gas.

### 3.1.2 Selection of a Differential Absorption Wavelength Pair

Calculations and simulations of the spectra associated with the absorption cross-sections of various atmospheric species across the UV, visible, and IR bands are performed by using atmospheric transmission modeling software. These spectra provide the starting point for the selection of the appropriate wavelengths to use to measure a gaseous species. Several criteria must be met in order to successfully perform a differential absorption measurement and require careful consideration when selecting absorption lines of the species. The availability of transmitter sources and minimal interference from overlap of additional species in the spectral region of interest are certainly the most crucial factors in the selection process. A MODTRAN$^{TM}$ 5 simulation in Figure 3-3 examines a region in the mid-IR from 4.5 – 4.6 μm, where several absorption bands of interesting species are present.

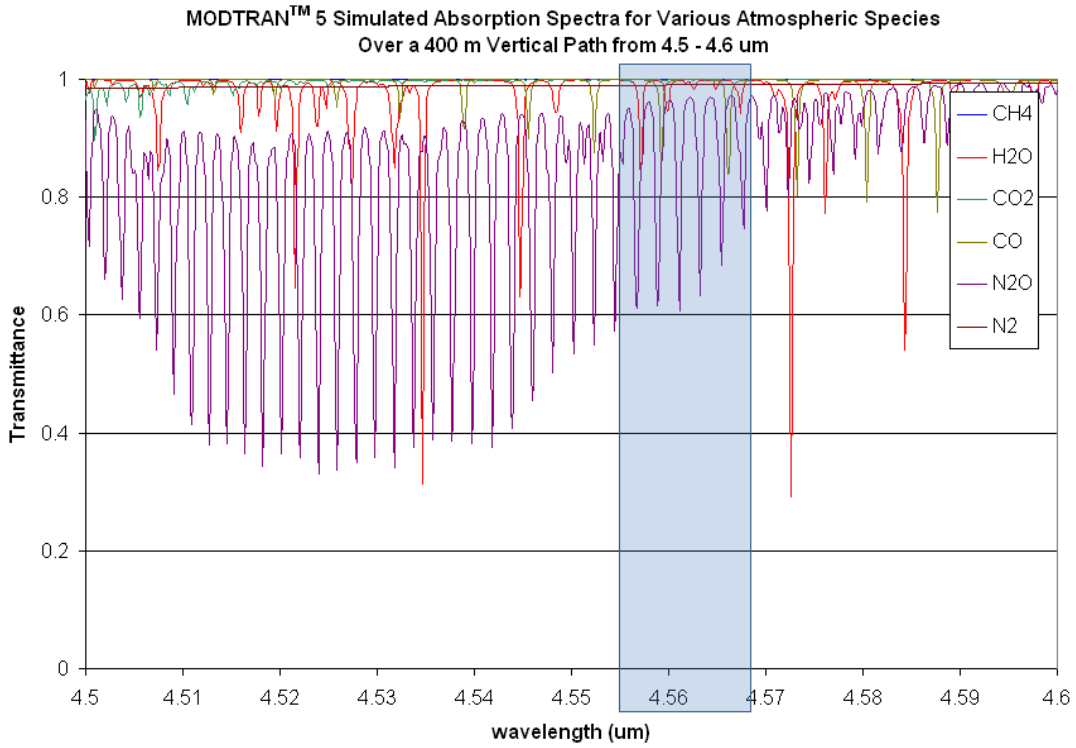


Figure **3-3**: MODTRAN™ 5 atmospheric transmission simulation in the mid-IR region of 4.5 – 4.6 μm showing absorption bands for various trace species; the highlighted region is expanded in Figure 3-4.

Nitrous oxide ($N_2O$) is the dominate absorption feature in the mid-IR spectrum presented in Figure 3-3; water vapor, carbon monoxide (CO), and carbon dioxide ($CO_2$) absorption lines are also present. Consideration of the spectral features present in this region require accurate differential absorption measurements at selected wavelengths and avoidance of interfering features, as outlined in the previous section. Assuming nitrous oxide ($N_2O$) is the species selected to be measured in this region, there are several lines at different wavelengths that can be considered to maximize sensitivity and performance of a differential absorption measurement. Since the average absorption feature width is on the order of 0.5 nm, lasers with linewidths of the same order (i.e. corresponding to ~ 0.5 $cm^{-1}$) in this region would be selected for measurements of $N_2O$. Figure 3-4 shows an

expanded region from Figure 3-3 that is selected to examine the spectra and optimize performance for an absorption measurement. While several other lines outside this selection possess greater absorption, those lines also occur in regions with overlapping absorption spectra. The selected lines for $N_2O$ in Figure 3-4 provide minimal overlap with other species without sacrificing sensitivity associated with absorption strength. Selection of wavelengths at the absorption features located near 4.5611 and 4.5632 μm are considered as primary online candidates and wavelengths near 4.562 and 4.564 μm would be good offline selections for an $N_2O$ differential absorption measurement.

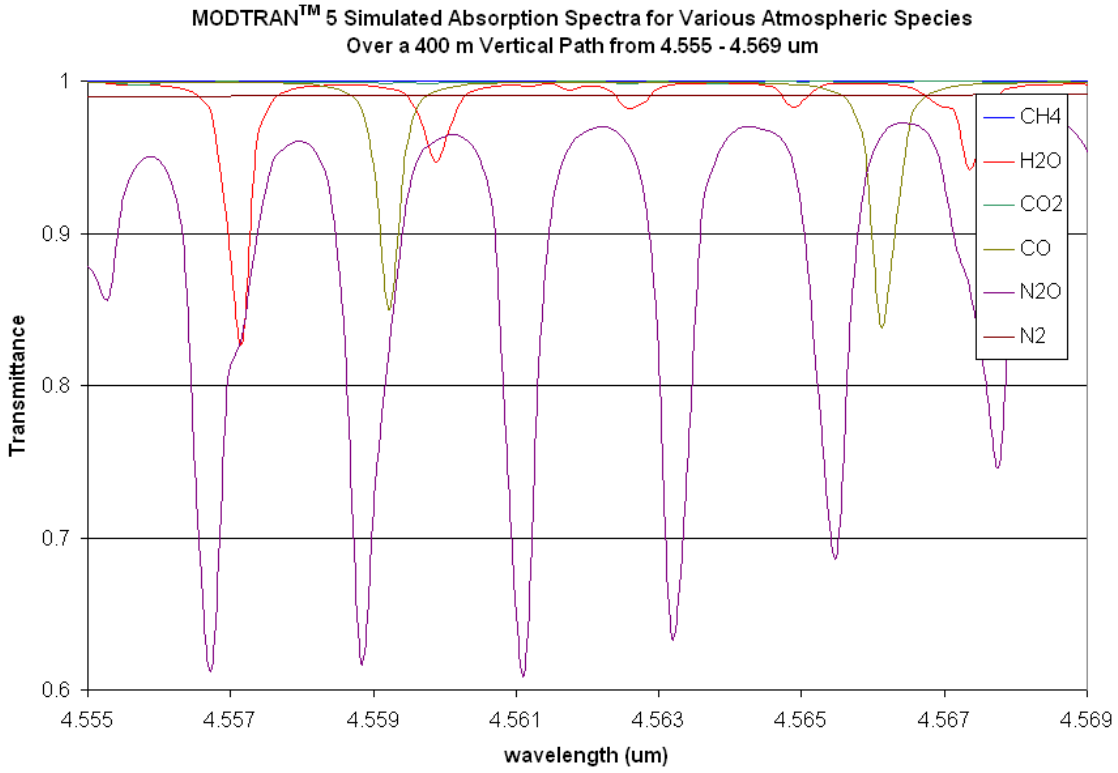


Figure **3-4**: MODTRAN™ 5 atmospheric transmission simulation in the mid-IR region of 4.555 – 4.569 μm show good choices of absorption lines for differential absorption measurements of $N_2O$.

### 3.1.3 Comparison of Techniques and Sources of Error

The modification and simplification of the lidar equation for calculating concentration path-length values on long path DAS configurations require only four parameters, which are based on system configuration, spectra consideration, and atmospheric conditions. These parameters are the range to the target (length of absorption path) the differential cross-section of the spectra, laser line shape compared with the species on-line wavelengths, and the ratios of the received on-line to off-line energies. However, there are several additional sources of error that may exist in systems implementing differential absorption techniques. Brown [2008], described five major contributions to noise and fluctuation in measured return signals. These include: (1) uncertainty in energy measurements including electronic noise and statistical error, (2) effects of path radiance and the ground or target reflectivity variations, (3) uncertainty in atmospheric optical depth, (4) the wavelength match of the online laser with the selected absorption feature, and (5) interference from additional atmospheric spectral features, such as optical scattering from the path or absorption by other species. Several of these contributions to error were analyzed as part of our work on system and algorithm development for the Airborne Natural Gas Emission Lidar (ANGEL) system operated by ITT Space Systems [Murdock *et al.*, 2008]. The ANGEL system uses a three wavelength DIAL/DAS sensor to detect natural gas pipe leaks and measure the concentration path length values. A number of advanced hardware and software techniques were developed to specifically address several of the error sources outlined by [Brown, 2008] including contributions from spectral mismatch on the absorption feature, spatial mismatch of the

on-line and off-line beam overlap functions on the hard target, and timing of transmitter/receiver pulse transmission/detection.

## 3.2 Broadband Absorption Measurement Techniques

The absorption spectra of many atmospheric trace species exhibit wide band absorption features in the UV, visible, and IR regions of the optical spectrum. The example spectrum in Figure 3-3 shows the absorption band of $N_2O$ spanning several hundreds of nanometers. Calculations using the HITRAN cross-sections show the fine scale structure and several spectra of species are shown in Figure 3-5. Broadband techniques, which use spectrometers to detect the species absorption, are able to measure these features and calculate results from differential absorption of multiple wavelength pairs. Sacrifices in sensitivity are made compared to the traditional DIAL approach of measuring wavelength pairs because the transmitter energy is spread over a range of wavelengths; however major advantages result from analysis of many on-line and off-line wavelength simulations and discrimation against interfering species. Traditional methods focus on two (or a few) wavelengths to measure the ratio between the on/off spectral features, as described in the previous section.

Several configurations of broadband spectroscopic systems have been used to demonstrate capabilities for detection of chemical species. Broadband sources used in these systems typically exist in two configurations: (1) ultra broadband sources in DOAS instruments, which use bright incoherent white light sources that span several hundred nanometers in wavelength, (2) broadband diode and laser sources, such as a super-

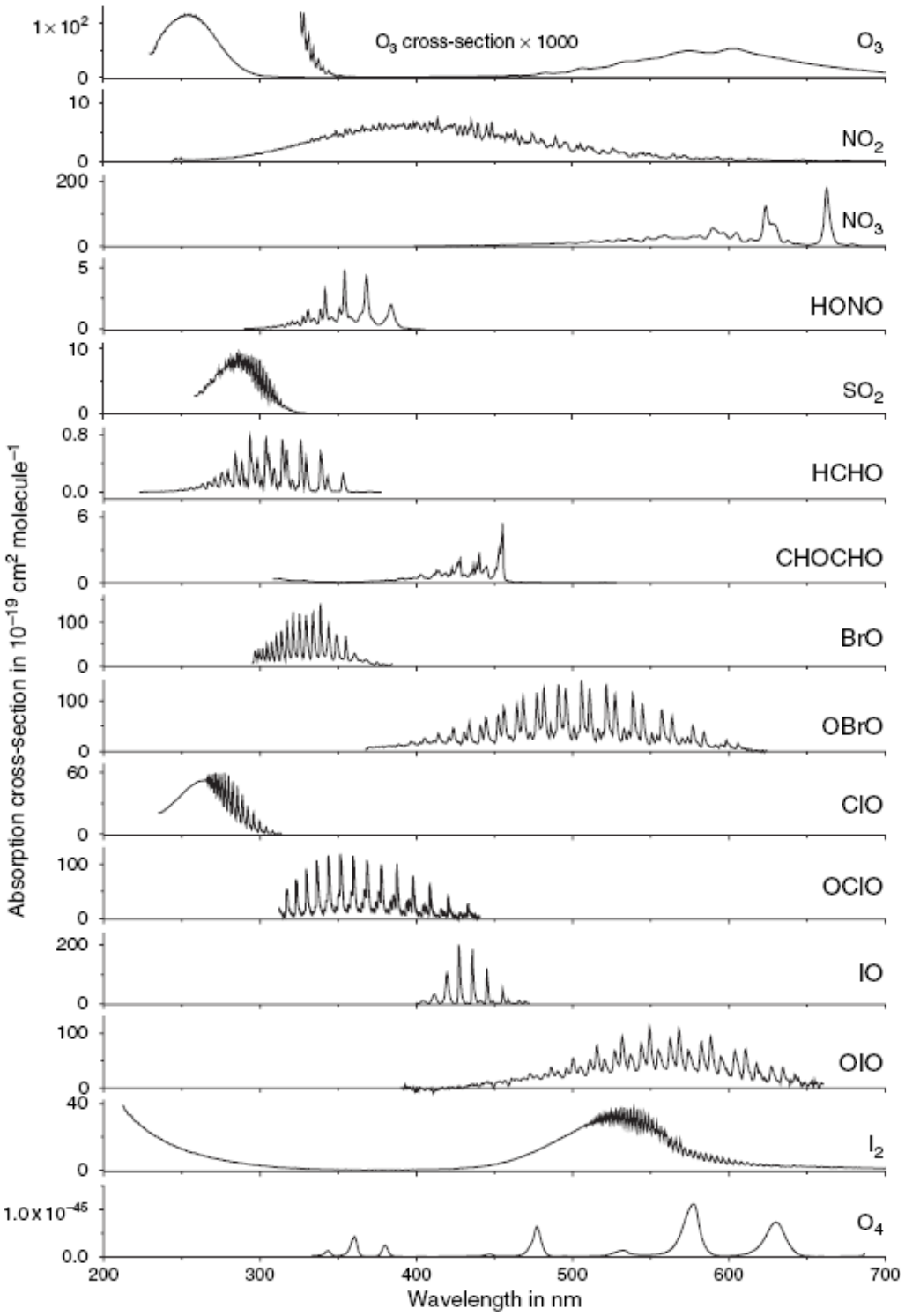


Figure **3-5**: Absorption spectra for many atmospheric species in the UV and visible. The widely varying structures allow for simple identification of each species [Figure from: Platt and Stutz, 2008].

luminescent light emitting diode (SLED), which is used for $CO_2$ absorption measurements at near-IR frequencies [Heaps, 2008], and the recent use of supercontinuum lasers [Begnoché, 2005; Brown *et al.*, 2008a and 2008b; Philbrick *et al.*, 2009; Edwards *et al.*, 2009; Wyant *et al.*, 2009]. These sources typically span several nanometers to hundreds of nanometers in wavelength range. The applications of the supercontinuum lasers to DIAL and DAS techniques are the primary focus of this research.

### 3.2.1 Supercontinuum Absorption Spectroscopy (SAS)

A supercontinuum laser source offers several advantages over other multiwavelength and broadband transmitter sources for obtaining differential absorption measurements of atmospheric species. A supercontinuum source provides spectrally broadband emission in the visible and infrared that is essentially continuous across a wavelength range of several hundred nanometers. Absorption features of multiple atmospheric species and overlapping interferents are observed simultaneously, and these are well resolved when coupled with a high resolution spectrometer or optical spectrum analyzer. Absorption spectroscopy techniques that implement the supercontinuum source are being developed at Penn State for applications that measure the concentrations of various chemical species in the atmosphere, and these techniques have been demonstrated over several hundred meter path lengths. Another major advantage of the supercontinuum laser over using typical narrowband lasers for DAS measurements is that

the questions related to the laser line position and the line shape relative to the spectral line of the species are eliminated.

#### *3.2.1.1 Creation of the Supercontinuum in Photonic Crystal Fibers*

Supercontinuum generation in photonic crystal fibers (PCF) is governed by several non-linear processes that convert single wavelength light into a broad spectrum. Factors controlling which non-linear processes contribute to the formation of the continuum include: the pulse length, pump peak power, the pump wavelength and the zero dispersion wavelength of the fiber. A femtosecond pump wavelength located in the normal dispersion regime of a PCF will generate continuum due to self-phase modulation and Raman scattering. As the pump source is moved closer to the zero dispersion wavelength, soliton self-frequency shifts contribute additional broadening [Alfano, 1989]. When the pump pulse length is sufficiently long (in the case of nanosecond Q-switched lasers), the dominant non-linear effect is phase-matched four-wave mixing. The four-wave mixing process creates higher and lower frequency light and depends on the pump power, the non-linear refractive index of the fiber, and the fiber effective area. If the pump power is sufficient, the newly created frequencies will self frequency shift through four-wave mixing, cascading until the broad supercontinuum is created, as shown in Figure 3-6 [Wadsworth *et al.,* 2004].

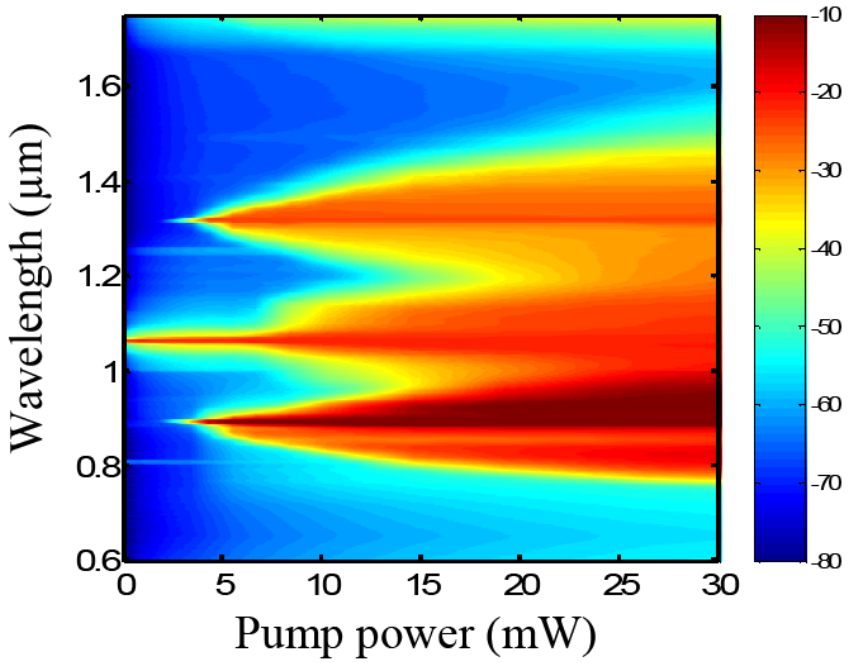


Figure **3-6**: The seeding of the signal and idler frequencies during the four-wave mixing process are shown at low pump powers in a PCF; at high pump powers the process has cascaded to provide a wide band spectral output (color bar values are in units of dBm) [Figure from: Wadsworth *et al.*, 2004]

### 3.2.2 Comparison of Techniques and Sources of Error

DOAS and SAS techniques have strong similarities in their broadband sensing capabilities. SAS is fundamentally a modification to the long established DOAS technique; replacing incandescent or xenon arc lamps with a supercontinuum laser as the broadband source. One particular advantage of the SAS is that the high intensity laser of narrow beam can be efficiently transmitted over very long paths. A comparison of the sources used for the different broadband techniques is shown in Table 3-1. Supercontinuum sources combine the brightness of lasers with the bandwidth typically provided by incandescent lamps spanning the visible to NIR portions of the spectrum.

The high brightness of the source provides increased capabilities for sensing minor atmospheric constituents across long path lengths.

Stability is a primary concern for broadband absorption measurements when operating at low power levels per wavelength interval, compared to high power discrete wavelength systems such as those described in section 3.1. DOAS lamps require ignition of a gas or a filament to generate light and are relatively stable processes, while the supercontinuum generation process undergoes several nonlinear processes to provide the broadband output. The nonlinear processes can often lead to significant amplitude variations and non-trivial amplitude fluctuations. The fluctuation noise is additive in integrated measurements. However, this noise can be overcome in supercontinuum systems operating at higher pump powers, which tend to increase the stability of the source.

Table **3-1**: Comparison of DOAS and SAS sources.

| measurement technique | DOAS | SAS |
|---|---|---|
| typical source type | incandescent or xenon arc lamps | supercontinuum laser |
| brightness | moderate | extremely high |
| coherency | no | yes |
| energy density | low | high |
| power requirements | high | low |
| propagation distance | few meters to several km | up to several km |
| wavelength span | UV to VIS, some NIR (<1200 nm) | UV-NIR, NIR-MWIR |
| stability of spectrum | high | moderate to high |
| flatness and smoothness | relatively flat and very smooth | can be extremely flat depending on configured non-linear processes |

## 3.3 Summary

Several differential absorption techniques exist for detection of chemical species in the atmosphere. The advantages of methods for differential absorption in multiwavelength DIAL systems and broadband DOAS configurations are combined in the development of an alternative broadband approach: supercontinuum absorption spectroscopy (SAS). The extremely broad spectral bandwidth and high brightness of the supercontinuum source enhance the detection capability of atmospheric species in several ways when compared to traditional atmospheric sensing systems.

# Chapter 4

# SAS Experimental Configuration and Hardware

The SAS instrument that was previously developed for measurements of atmospheric constituents [Brown *et al.*, 2008a and 2008b] is now improved to operate over path lengths of one kilometer or longer. The optical configuration and performance of the SAS system are described in this chapter.

## 4.1 Configuration of the Transceiver System

The configuration of the SAS system permits operation on a folded path length of 890 m between the rooftop of the Electrical Engineering East (EEE) building located on the Penn State campus, and the upper deck level of a parking garage located in the downtown portion of State College, PA. The system makes use of several components similar to classical atmospheric lidar configurations; a laser transmitter is configured with a beam expander to reduce the beam divergence for long path propagation, a receiving telescope is used to collect the backscatter and/or the scattered return from a target, and a detection system capable of measuring the return signal is used to measure the signal intensity as a function of wavelength over a selected spectral range. In the case of SAS, the spectral discrimination of the detection system is obtained using a optical spectrum analyzer or a grating spectrometer.

Figure 4-1 shows the optical layout of the transceiver system and Figure 4-2 shows a photo of the setup located in the rooftop laboratory of the EEE building. The outgoing beam is directed by three mirrors (M-1, M-2, M-3) and steered by a large micro-adjusted "kite-shaped" mirror (M-4). To maximize signal return, a 6 inch diameter corner cube retroreflector (M-5 in Figure 4-1) is placed at the target on the distant rooftop location and positioned to capture the transmitted beam. The retroreflector returns the beam back along the axis of the transmitted beam thereby coaxially aligning the transmitted and received beams. The return beam is captured by the receiving telescope (10 inch Newtonian) which focuses the return beam with reflective optical elements (M-6, M-7). The focused return beam is collimated by a short 25 mm focal length lens (L-1)

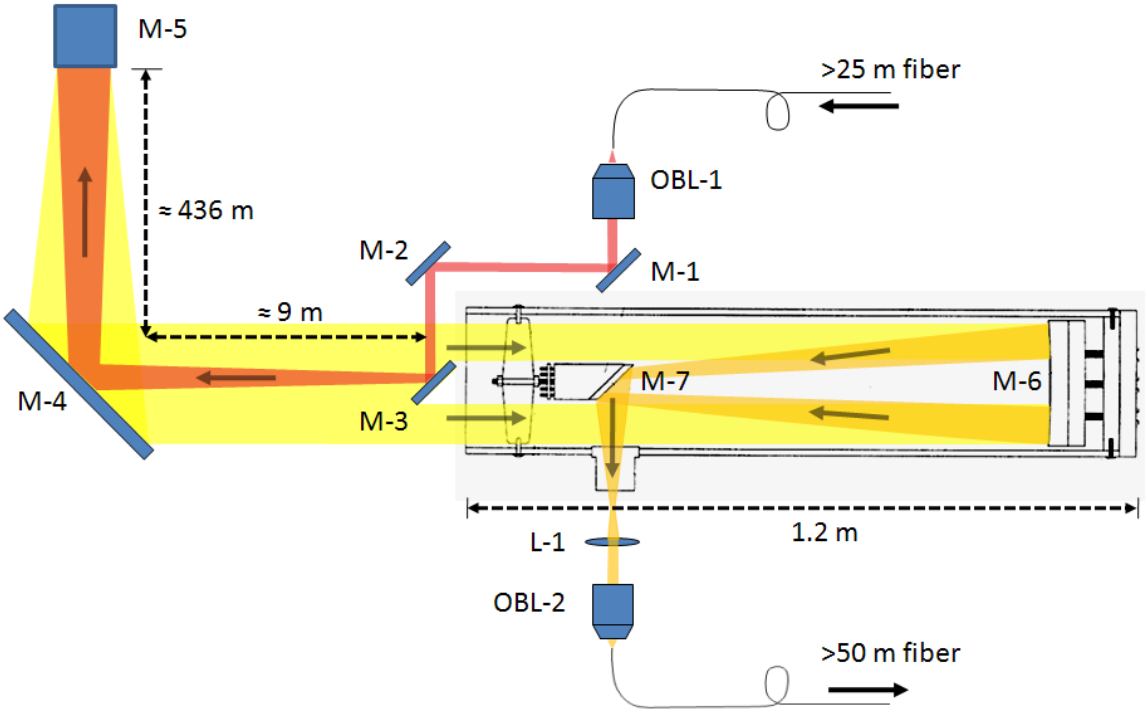


Figure **4-1**: Configuration of the transceiver system located in the rooftop laboratory of the Electrical Engineering East building on the Penn State campus. Optical elements M-x are mirrors, OBL-x are objective lenses, and L-1 is a biconvex lens. M-5 is a corner cube retroreflector located on a distant rooftop completing the 890 m folded path. Mirrors M-6 and M-7 form a Newtonian telescope configuration.

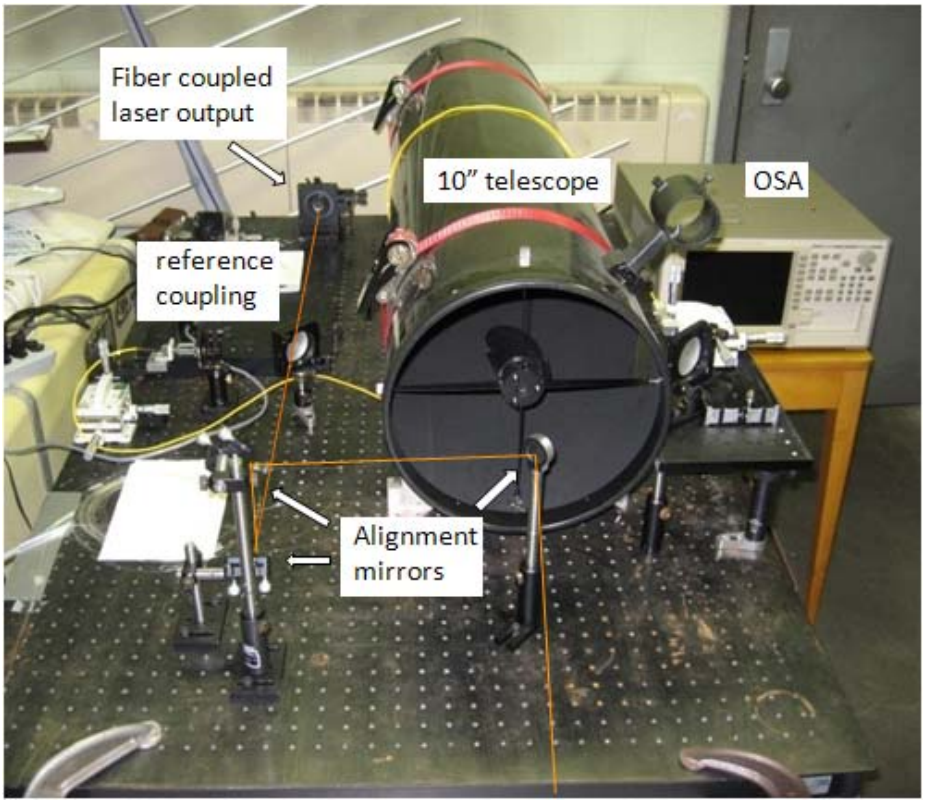


Figure **4-2**: Picture of the rooftop transceiver system with the outgoing path highlighted.

before refocusing into a fiber by an objective lens (OBL-2). The layout and alignment of the steering mirrors, retroreflector, and telescope result in a coaxial, folded path that aligns the transmitted and received beams. Furthermore, the folded path methodology permits co-location of the transmit and receive portions of the system; thus minimizing the amount of hardware deployed at the target location. Each of the components in the system are further defined in Table 4-1, where information on the type of mount, physical properties, and manufacturer part number is provided.

Table **4-1**: Optical components used in the transceiver portion of the SAS system are identified with components shown in Figure 4-1.

| Label | Component | Mount Type | Physical Propert. | Part # if avail. |
|---|---|---|---|---|
| M-1, M-2, M-3 | alignment mirrors | two-axis pitch and yaw mirror | 1" first surface | Newport 10D20ER.2 |
| M-4 | Turning mirror, kite shape | custom two-axis pitch and yaw | 14" first surface | Anchor Optics AX27112 |
| M-5 | Corner cube retroreflector | Tripod with yaw, pitch, and roll adjust | 6" aperture, three gold flashed surfaces | N/A |
| M-6, M-7 | Newtonian telescope | custom fixed-movement, horizontal | 10"aperature, 1.08° FOV, f/# = f/5 | Celestron Starhopper 10 #10110 |
| OBL-1 | Collimating objective lens | two-axis pitch and yaw, threaded | 5x magnification/ 0.1 NA | Newport M-5X |
| OBL-2 | Focusing objective lens | two-axis pitch and yaw, threaded | 40x mag. 0.65 NA | Newport M-40X |
| L-1 | Collimating lens | Two-axis pitch and yaw mirror | Biconvex, 25 mm Dia., 25 mm FL | N/A |

The transceiver portion of the system is optically coupled by long single mode fibers (SMF) to the source and detector portions of the SAS system, since they are remotely located in two separate laboratories in the Electrical Engineering East building. The source (supercontinuum laser) is located in a third floor laboratory just below the roof top laboratory and the detector (high resolution spectrometer) is located in a basement laboratory. The motivation for the fiber optic coupling of the source, transceiver, and detector portions of the system is primarily due to the distribution of shared resources which are also used for experiments unrelated to this work. The long length fibers used for the coupling configuration introduce some additional complexities to the system from added noise in the measurements and this topic will be discussed in the following sections. However, the fiber coupling approach is compatible with the fiber laser transmitter source, and with the several types of detector systems. Therefore,

the system configuration is appropriate for use in future instrument designs, including those with co-located source, transceiver, and detection systems using reduced fiber lengths.

## 4.2 Configuration of the Supercontinuum Source

A supercontinuum fiber laser source is used as the transmitter in the Penn State SAS system. An 18-m length of photonic crystal fiber (SC-5.0-1040, Blaze Photonics) is coupled to a nanosecond 1064 nm laser (JDSU NP-10620-100), which delivers 40 mW average power. A Newport 461-series three-axis translation stage provides efficient coupling of the laser to the fiber via a 60x microscope objective. Nearly 18-mW of laser power is spread across several hundred nanometers at the fiber output via the nonlinear pulse broadening processes discussed in section 3.4. Figure 4-3 shows an overview of the supercontinuum laser setup.

The supercontinuum output at the end of the photonic crystal fiber is focused by a 10x objective lens to effectively collimate the output. The objective lens also provides a collimated beam to fill the full aperture of another objective lens used to refocus the light into the single mode fiber that transfers the output to the rooftop transceiver system. Two mirrors are used to align the beam and optimize coupling between the two objective lenses.

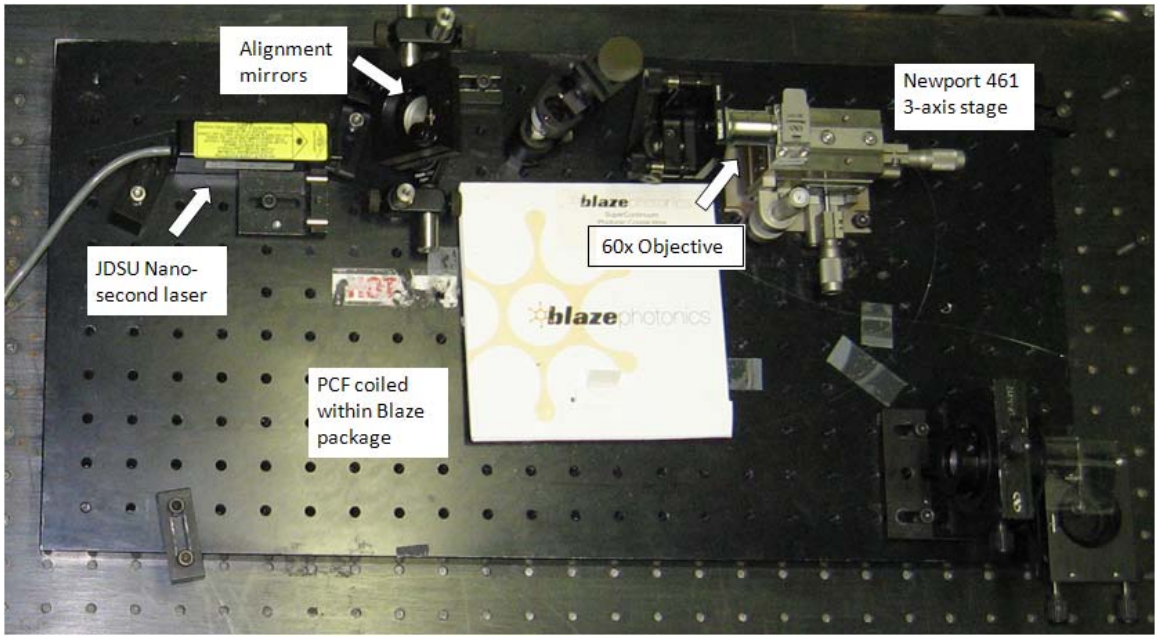


Figure **4-3**: Configuration of the supercontinuum source. The PCF is coiled in the Blaze Photonics packaging for protection.

### 4.2.1 Spectral Bandwidth

The supercontinuum source described in section 3.4 transmits a broad spectrum of several hundred nanometers. The source spectra for the laser configuration used in the measurements reported in this work is similar to the spectral measurement reported previously [Brown *et al.*, 2008b]. The previously reported spectrum presented in Figure 4-4 (a) shows the broad nature of the source, with a relatively flat spectrum across portions of the visible and NIR. This spectrum was recorded directly from the output of the PCF fiber. Figure 4-4 (b) is the measured spectra from the output of the single mode fiber measured at the rooftop transceiver used in this research. The overall structure is found to be similar in Figure 4-4 (a) and in Figure 4-4 (b); however, noticeable differences across the wavelength span exist. The spectrum exhibits significantly more

variation in power. This variation in spectral smoothness provides an added complication for analyzing measurements of absorbing species. Minimization of the non-uniformities across the spectrum is attained by time integration to reduce the amplitude of random variations in the received spectra. By implementing the fiber filtering techniques described in section 4.4.3 the variations are further reduced.

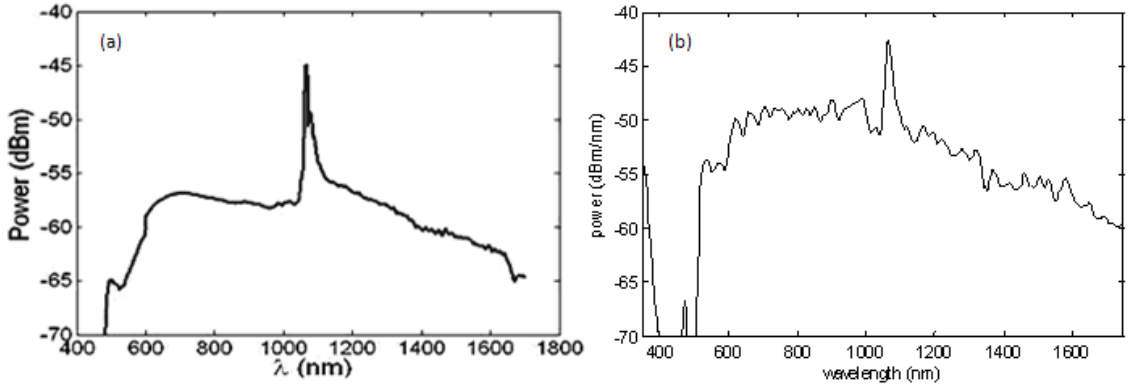


Figure **4-4**: (a) Measured supercontinuum power spread at the PCF fiber exit after a neutral density filter in dBm [Brown *et al.*, 2008b] and, (b) measured supercontinuum output after 25 m of SMF-28 fiber.

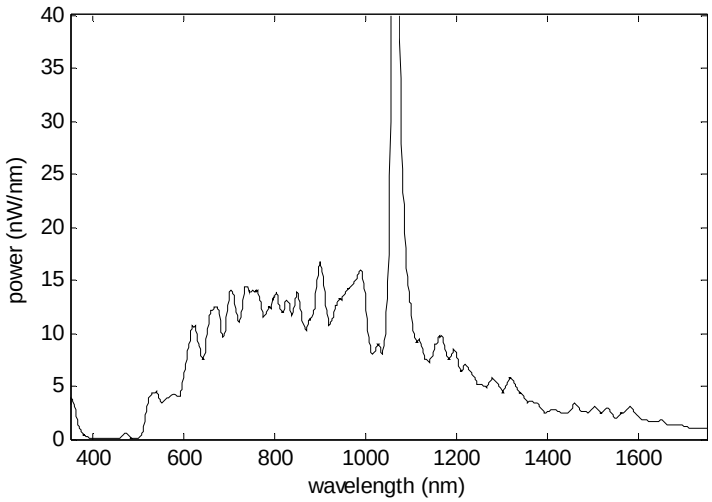


Figure **4-5**: The Supercontinuum output power at the exit aperture of the rooftop end of the SMF-28 fiber, in nW/nm.

## 4.3 Alignment of the SAS System

The SAS system is aligned by adjusting several optical elements located in the transmitting and receive paths. The alignment procedure for the components along the path is discussed in this section.

### 4.3.1 Components for Alignment

The long path length (890 m) used for the absorption measurements reported in this work requires alignment optics capable of performing precision location adjustments on the transmitted beam. The components for collimating the outgoing beam remain fixed while fine tuning of the alignment mirrors and the 14 inch turning mirror provide sufficient beam steering capability. The transceiver arrangement, similar to Figure 4-1, is shown in Figure 4-6 as a three dimensional depiction highlighting the folded atmospheric

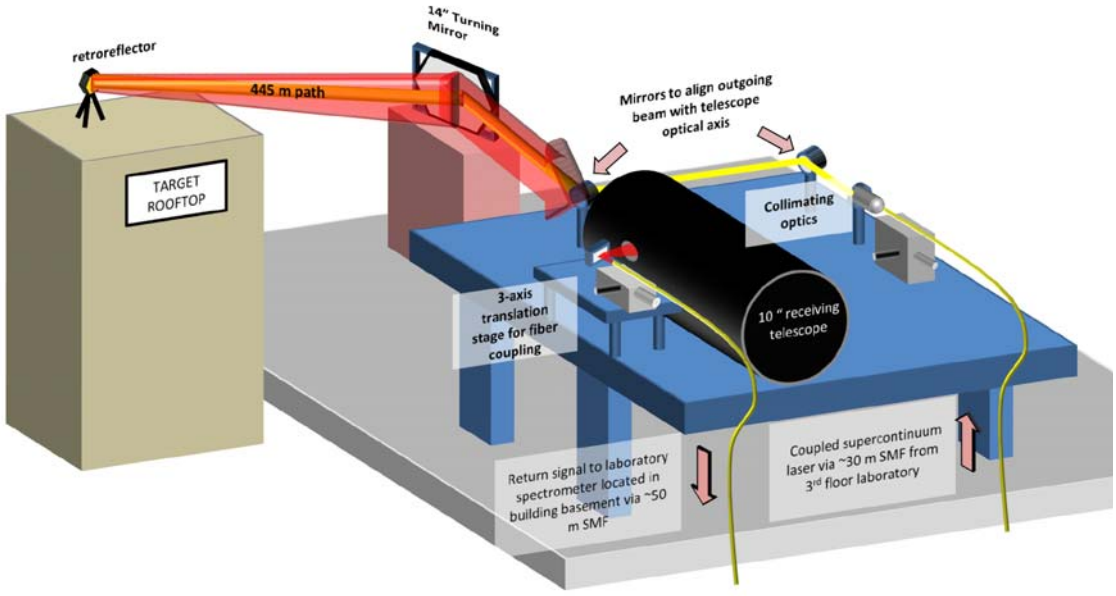


Figure **4-6**: A 3-D pictorial shows the rooftop transceiver arrangement located on the Electrical Engineering East building on the Penn State campus.

path and location of the various components of the system. The retroreflector creates the folded path return and eliminates the need for fine adjustment of the beam by virtue of its inherent retro-reflection properties (parallel incident and reflective beams). Overall, the configuration of the optical elements provides a safe and effective means for alignment and control of the beam across the several hundred meter path. The procedure and methods for alignment are further discussed in the following section.

### 4.3.2 Transmission Path and Retroreflector Placement

The transmission path is extended significantly compared with previous configurations of the SAS system and provides a longer integrated path length with increased sensitivity for atmospheric trace species as well as for the primary constituents. Figure 4-7 shows the path utilized previously for measurements over 300 m (and 540 m with an added folded path) between the rooftops of two buildings on the Penn State campus, and the extended path over roadways and buildings of downtown State College. The retroreflector is temporarily mounted during measurement periods on the rooftop of a parking garage approximately 445 m away from the rooftop laboratory on the EEE building; thus completing the 890 m folded path configuration described.

Measurements of the path length depend on the accuracy of an infrared range finder used to obtain measurements of those portions of the path greater than 20 feet. The range finder has a maximum range of 450 yards and an accuracy of ±1 yard (± 0.91 m). The configuration of the path requires three lengths for measurement, two of which

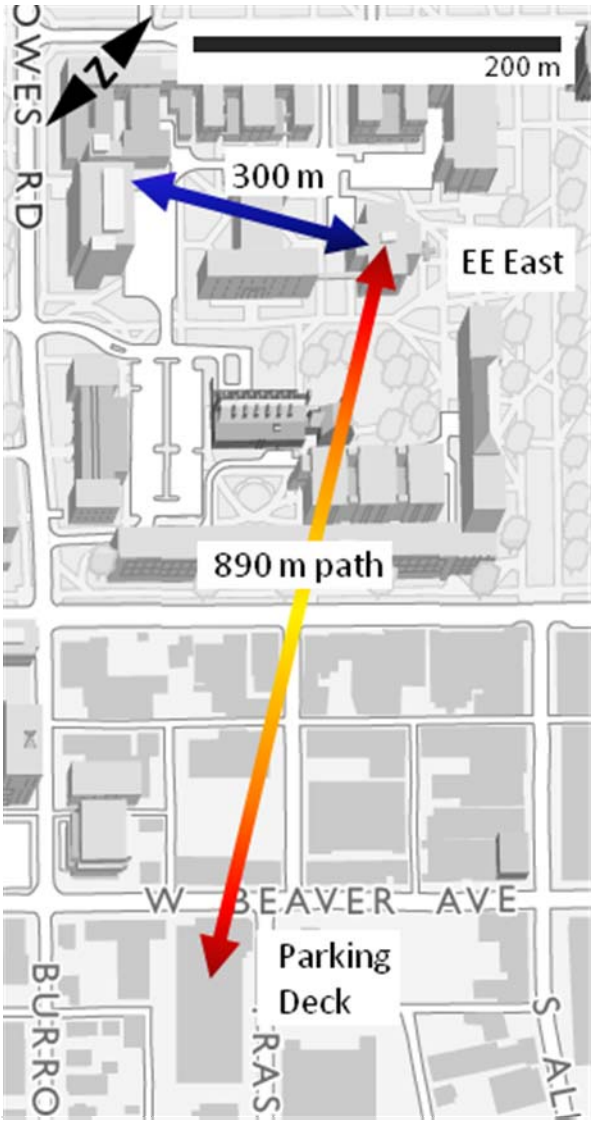


Figure **4-7**: Path configurations across the Penn State campus and downtown region of State College, PA.

are measured by the range finder. The first length, between the transmitting mirror (M-3 in Figure 4-1) and the large turning mirror (M-4 in Figure 4-1), is measured with a tape as 8.79 ± 0.05 m (346 ± 2 in.). The second portion of the path, measured from the turning mirror to the target rooftop's side facade using the range finder, is 373.07 ± 0.91 m (408 ± 1 yd.). The latter measurement required several attempts to be successful, as the

alignment of range finder with the target facade proved difficult. The final path measurement from the target rooftop façade to the retroreflector position is measured using the range finder to be 63.09 ± 0.91 m (69 ± 1 yd). Overall, the total path length resulting from the addition of the measurements results in 444.9 ± 1.3 m to provide a folded path of 890 m, see Figure 4-8.

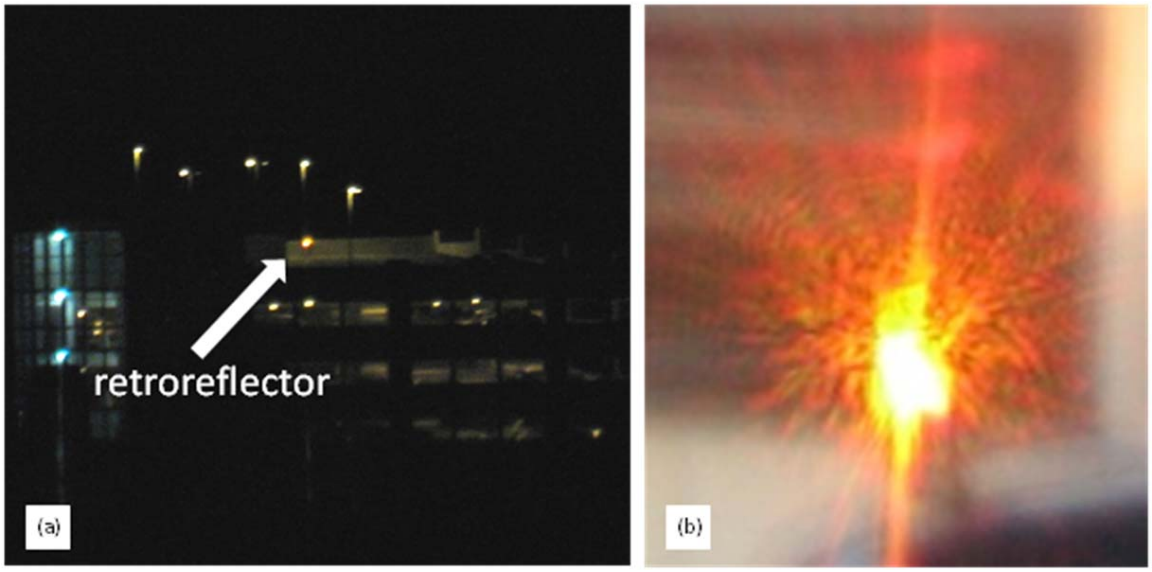


Figure **4-8**: (a) View of the location of the corner cube retroreflector as seen from behind the turning mirror (M-4 in Figure 4-1) located on the rooftop of the Electrical Engineering East building on the Penn State campus. (b) A view of the retroreflector through the 10" telescope during early morning hours towards the end of a night of measurements.

### 4.3.3 Method for Beam Alignment

Alignment of the rooftop transceiver is required before each operation of the SAS system. With the laser operating at low power, the alignment mirrors are configured to position the beam in the approximate direction of the telescope's field of view. The telescope receiving optics are temporarily replaced with the stock secondary eyepiece to

permit viewing of the spot location of the laser impinging on the rooftop brick wall of Electrical Engineering West located at approximately 75 m distance. The mirrors directing the outgoing beam are adjusted to center the laser spot in the field of view of the telescope. This method provides an approximate coaxial alignment of the telescope receiver and transmitter.

After the on-axis alignment is complete, the laser output is shuttered and the turning mirror is replaced in its operating location. The turning mirror is now viewed through the telescope eyepiece which directs the viewing path towards the parking garage. Rough alignment is completed by adjusting the turning mirror to fill the field of view of the telescope with an image of the parking garage rooftop, where the retroreflector is located. Micro-adjustments to the turning mirror are made to approximately center the location of the retroreflector image in the telescope field of view. This completes the initial alignment of the transceiver along the folded path.

Fine adjustments are made to prepare the system for measurements. The laser is switched on to transmit along the optical path to illuminate the retroreflector. Small adjustments to the laser alignment mirrors are often necessary to completely fill the retroreflector. The return signal projected through the eyepiece port is imaged on a white background, such as white printer paper; see Figure 4-9 (a). The hexagonal image is indicative of the real and reflected edges of the cube retroreflector. If the image intensity is non-uniform small adjustments made to the collimation of the transmitted beam and the alignment mirrors correct for this effect.

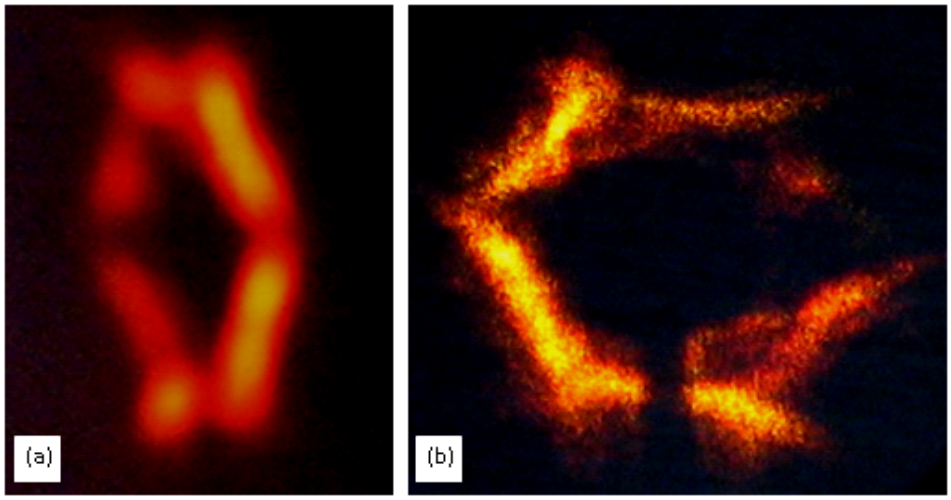


Figure **4-9**: Return beam imaged and viewed at a side angle on white paper (a), and on (as seen through the backside) the surface of clear adhesive tape (b).

## 4.4 System Performance and Efficiency Estimations

The SAS system is capable of acquiring measurements of several prominent absorption bands in the visible and NIR regions, over path lengths approaching 1 km. The relatively strong NIR absorption bands from approximately 600 to 1400 nm are in the spectral region with the highest power per wavelength interval in the bandwidth of the supercontinuum laser. However, SAS measurements are distorted by noise, which originates within the system, as well as the effects of transmission through turbulence along the open path. Different irregularity features exist in both the transmitted and received beams that affect the accuracy of the measurements. The sources of these irregularities and their effects are discussed in the following section.

### 4.4.1 Long Path Supercontinuum Beam Propagation

Propagation of a laser over long path lengths is easily achieved by expanding to collimate the laser beam. The beam expander optics are configured for efficient operation at the laser wavelength, producing an output beam size related to the beam expansion ratio. The beam divergence is also effectively reduced by the factor of the expansion ratio. However, in the case of using refractive optics with a broadband supercontinuum laser source, this technique is limited by the changing focal length as a function of wavelength for propagation over long path lengths.

A supercontinuum source using stationary refractive optics is only capable of optimal collimation at a single wavelength. When using wideband supercontinuum lasers, the spectra furthest away from the designed collimation wavelength will diverge more quickly with distance than the portion near the configured collimation wavelength. For instance, on short paths over a couple meters on a laboratory optical bench, the collimation wavelength is best chosen at the center wavelength of the broadband source to minimize divergence across all wavelengths. However, on longer paths of 100 meters or more, the collimation point should be adjusted to optimize for the spectral region of interest, because the divergence will be observed more strongly at larger distance.

Figure 4-10 demonstrates the wavelength divergence effect. The spectral bandwidth of the supercontinuum laser is divided into one hundred operational wavelength intervals and a Gaussian beam is simulated propagating over an 890 m path. The plots show calculations of the intensity cross–sections in the plane of the Gaussian beam as a function of wavelength at a range from after expanding the beam to diameter

of 1 cm and 1.5 cm at the beginning of the path. The intensity values are shown by the color bars. The Gaussian beams shown in Figure 4-10 are expanded to their initial propagation sizes by collimating the beam at the 750 nm wavelength, then expanded by the beam expander configured with the desired expansion ratio. The beam expansion is calculated for the case of an initial 5 mm diameter laser beam. The simulations are run for propagation over a clear atmospheric path neglecting refraction, absorption and turbulence in the atmosphere. The simulation shows the distribution of the power per wavelength increased at longer wavelengths; in Figure 4-10 (a) at 1.75 μm the spot size is greater than 120 mm compared to the spot size at 0.35 μm of roughly 40 mm. Furthermore, the power at the central point of the 1.75 μm operating wavelength is reduced to less than 20% of the initial output power whereas the 0.35 μm operating wavelength beam still contains greater than 55% of the initial power per wavelength compared with the central portion of the beam.

Figure 4-10 (b) is configured with an initial output beam width increase of 50% over the beam width used in 4-10 (a) by changing the beam expander ratio (1.0 cm to 1.5 cm output beam size). This significantly increases the Rayleigh distance (transition point from near- to far-field) for the collimated source, and reduces the divergence of beam across all wavelengths. By expanding the size of the output beam, significantly more power is maintained within the center portion of the beam at longer wavelengths. Figure 4-11 shows a comparison of the full width half maximum (FWHM) values from the two simulations in Figure 4-10. The FWHM values for the 1.5 cm initial output beam at shorter wavelengths are comparable to the 1.0 cm beam's FWHM values; however, at

longer wavelengths the FWHM values of the 1.5 cm beam are significantly less than the 1.0 cm values, as expected for the larger beam expansion.

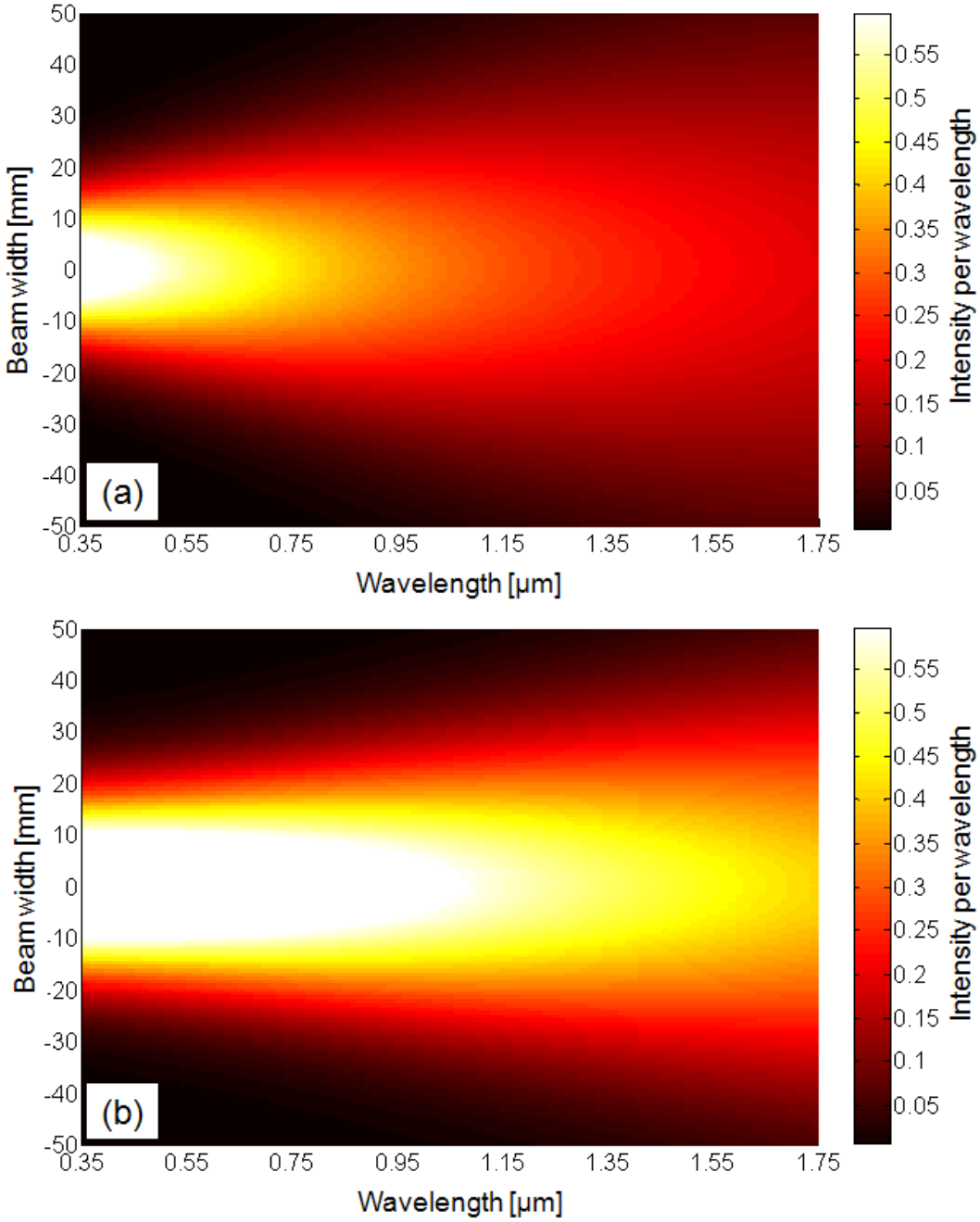


Figure **4-9**: Simuations for intensity distribution of a gaussian beam 890 m down range per wavelength (0.35 – 1.75 μm) for (a) 1.0 cm initial output beam and (b) 1.5 cm output beam.

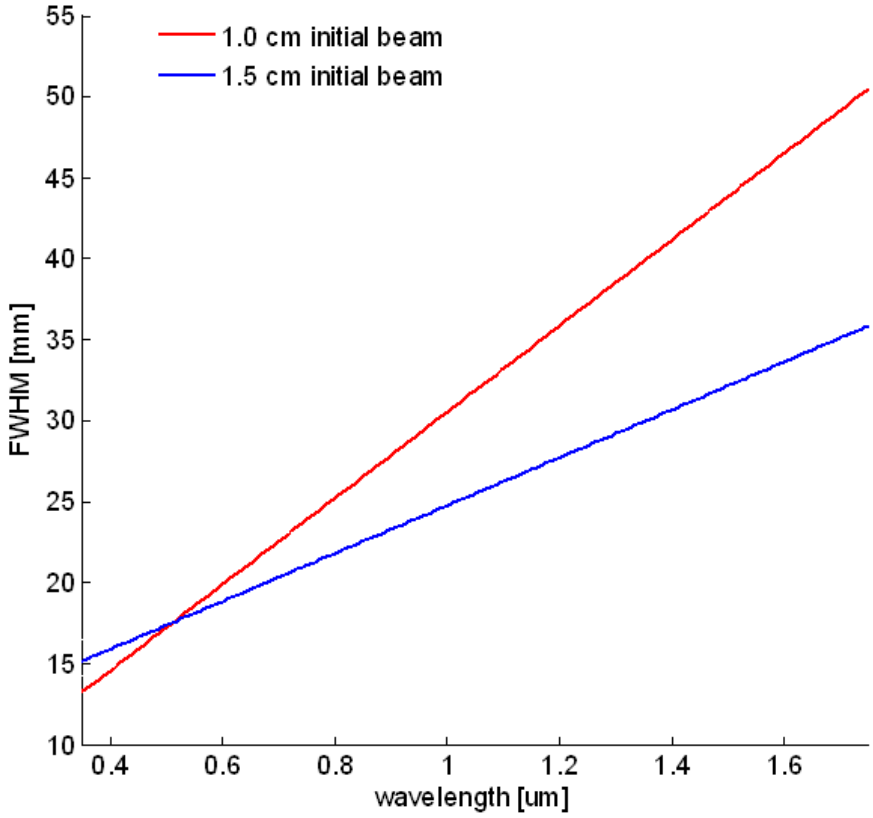


Figure **4-10**: Simulated beam spread for propagation of a Gaussian beam at 890 m down range for a 1.0 cm initial output beam and a 1.5 cm beam.

Based off the simulations in Figure 4-10 and 4-11, it is shown that increasing the transmitted laser beam width will significantly reduce the spot size over a long path. On the other hand, an increase in beam width requires the use of larger optics, and more attention to minimizing the aberration effects introduced by a beam expander configuration. In the experimental configuration of SAS, the beam is expanded to approximately 1 cm to fit easily within the 2.5 cm diameter optics. This configuration of the beam provides sufficient signal return for the spectral regions of interest. However, measurements further into the NIR will require more attention to the details described in this section.

### 4.4.2 Fiber Coupling of Source and Detector

The fiber coupling of the spectrometer located in the basement and the third floor supercontinuum laser to the rooftop transceiver system causes the majority of losses in the efficiency of the transmitted and received signals. Focusing the collimated supercontinuum laser beam into the Corning SMF-28 fiber via a 40X objective lens typically results in approximately 3 dB loss. Therefore, with the supercontinuum yielding 12-18 mW power, the coupling into the single mode fiber will provide approximately 6-9 mW at the rooftop transceiver. However, during several of the measurements presented in Chapter 5, additional losses in the system resulted in transmitted powers of only about 3-4 mW at the rooftop end of the single mode fiber.

### 4.4.3 Modal Noise in Coupling Fibers

The SMF-28 fibers used to couple the rooftop transceiver portion of the SAS system are single mode fibers intended for operation at wavelengths longer than 1200 nm. At shorter wavelengths, the diameter allows additional higher order modes to propagate through the fiber. For the long fibers used in coupling our configuration of source and detector to the rooftop lab portion of the system, higher order modes do occur. These produce increased noise levels, which are observed by the grating spectrometer in the visible and NIR spectral regions of interest.

The modal noise is non-uniform and non-random, and varies according to the positioning of the long length fiber. Commercially available mode mixers/scramblers and mode filters work to minimize the non-uniformities and randomize the modes to

normalize the noise induced on a spectral measurement. These devices work on the principles of macro- and micro-bend losses, which limit propagation of short wavelength components by minimizing high order mode distribution in a multimode fiber. In multimode fibers, the number of propagation modes is reduced as a function of the bend radius applied to the fiber.

The commercially available fiber filtering devices are optimized to operate in specific wavelength regions, typically at the telecommunication bands. Therefore, we have developed our own in-house filtering techniques to mitigate the modal noise developed in the long length coupling fibers used for the SAS system to improve absorption measurements in different portions of the spectrum. The filtering technique, first utilized by Brown [2008], involves bending and twisting the fiber simultaneously to create a range of bend radii, which induce macro and micro bend losses. The bend radii used ranged from a few millimeters to a couple of centimeters. During a measurement integration period, both the transmit and receiving fibers are manually subjected to the bending and twisting on selected locations along the jacketed portions of the fiber. Operating on the jacketed fiber ensures the fiber is protected during the handling process. This technique of combining bending and twisting of the fiber results in a more uniform distribution and reduces the modal noise through loss of the high order modes. Without using this filtering technique, modal noise dominates the measured spectra, and significantly reduces the ability to analyze differential absorption measurements in our operating range.

### 4.4.4 Summary of Total System Losses

The low-level light measurements conducted by atmospheric sensing systems requires an understanding of the optical efficiencies of the system elements. The multiplicative nature of the losses at each of the optical elements along the transmit and receive paths significantly reduces the overall efficiency for the optical configuration. Table 4-2 lists the individual losses for each element in the SAS system, and provides the efficiency for the entire system in the visible and NIR. Approximately 5-7% of the

Table **4-2**: Estimated power efficencies for the SAS system. Several of the components optical efficiencies are reported from their respective datasheets, estimations based on typical incident and reflected/refracted power measurements, or calculated**.**

| Component | Individual transmission [efficiency %] | | Total transmission [efficiency %] | |
|---|---|---|---|---|
| | Visible | NIR | Visible | NIR |
| ER.2 Mirrors (x3 on transmit side) [datasheet] | 97 | 93 | 81 | 92 |
| 14 in. turning mirror (x2 along folded path) [datasheet] | 85 | 85 | 72 | 72 |
| Retroreflector [estimated Al. reflective] | 85 | 85 | 72 | 72 |
| Telescope optics (two mirrors) [estimated Al. reflective] | 85 | 85 | 72 | 72 |
| Fiber coupling inputs (x1, includes focusing optics) [estimated] | 50 | 50 | 50 | 50 |
| Fiber collimation (x2 collimators) [estimated] | 90 | 90 | 81 | 81 |
| Power loss from retroreflector overfill [estimated] | 50 | 50 | 50 | 50 |
| Fiber propagation length losses (both coupling lengths) [estimated from datasheet] | 92 | 97 | 92 | 97 |
| ESTIMATED SYSTEM EFFICENCY | | | 5% | 7% |

transmitted power in the SAS configuration is expected to be received at the spectrometer input based off this simple estimate of system efficiency. The estimate is based on the optimal efficiencies of all elements, and represents a best case scenario. The actual measurements of the average returned signal power at the spectrometer input were found to be much lower, around 0.5 to 3% of the transmitted power.

## 4.5 Summary

The SAS system described in this chapter is a modification of previous generations of the system that is designed to operate over longer paths while maintaining its' capability for visible and NIR absorption measurements of atmospheric species. The complexities for operating over the extended path are addressed; including alignment techniques, collimation of the supercontinuum beam, and fiber coupling of the transmitter and detector portions of the SAS system.

# Chapter 5

# SAS Long Path Measurements of Atmosphere Species

Long path absorption measurements of atmospheric constituents obtained using the SAS system are described in this chapter. These measurements include NIR absorption spectra of atmospheric oxygen and water vapor from March and April 2009 measurement campaigns. The measurements, along with a description of the data analysis techniques, are presented in this chapter.

## 5.1 SAS Analysis Techniques

The raw NIR spectra measured by a high resolution CCD grating spectrometer contain the features showing absorption by atmospheric species of interest. However, the spectral data require several steps of analysis to prepare for qualitative and quantitative results to compare with simulated absorption data. Qualitative comparisons are made with high-resolution MODTRAN$^{TM}$ 5 transmission spectra, which are calculated for the same conditions of path length, effective slit width of the grating spectrometer, and atmospheric conditions at the time and location of measurement. After qualitative agreement with the MODTRAN$^{TM}$ simulations is examined, the data is processed using a multiwavelength differential absorption inversion algorithm previously developed by Brown *et al.* [2008b]. The inversion algorithm utilizes temperature and pressure broadened HITRAN spectra to calculate the differential absorption. The algorithm iterates over several hundred wavelengths to derive a CPL value for the absorbing species

concentration. These analysis techniques are further discussed in the subsequent sections.

### 5.1.1 Data Analysis Procedure

The raw experimental data possess features that include instrument sensitivity and response functions as well as measured system noise. These features are often nonlinear and non-uniform across the data set, and require curve fitting routines to remove or correct for their presence. Reference background spectra and spectra of the laser source scattered from a near field diffuse target are taken near the time of measurement to provide inputs for curve fitting routines and corrections. These routines provide instrumental corrections that are applied to the experimental data.

The near-field reference spectra are captured using all the optical components of the SAS system except the retroreflector. The large turning mirror is used to redirect the transmitted beam over a short path (< 2 m) back through the receiving telescope, thus mimicking a return signal. The telescope focuses the signal into the long SMF fiber connected to the grating spectrometer, as described in Chapter 4. While this technique introduces a small amount of absorption in the reference path, the levels are sufficiently small, compared with the long path , that their contribution approaches the noise level in the measurement. Therefore, the reference data is accepted and used in correcting the raw primary optical absorption data.

Figure 5-1 shows reference spectra and curve fits of the reference spectra overlaid with the raw experimental data. The background is subtracted from the reference spectra

and the raw experimental data; however, this is the only factor applied to the raw data shown in Figure 5-1. The background subtraction data are obtained by integrating the background "dark" noise of the spectrometer laboratory over a similar time interval, and near the time of the measurements. This correction is necessary since the spectrometer is free space coupled to the signal fiber, making it susceptible to interference by other sources. Furthermore, it is necessary to background subtract the system reference, as well as the experimental data, since the near field reference signal is much more intense

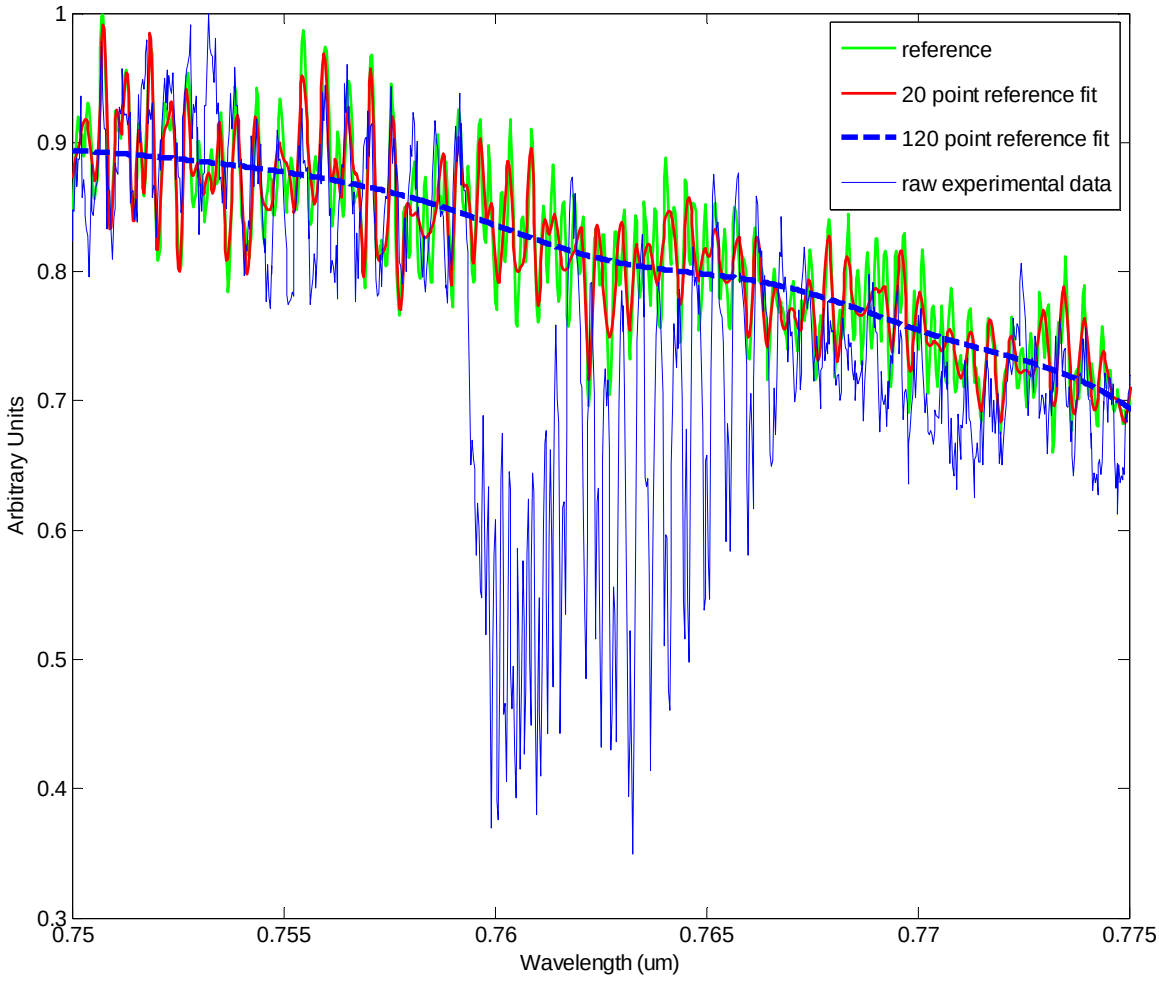


Figure **5-1**: Reference spectra fits (20 point and 120 point) used in the analysis algorithm, which is applied to the raw experimental data, are plotted for the spectral region of an oxygen absorption feature.

than the data signal and it requires different scaling coefficients. In the figure, the two reference fit curves represent “high” frequency and “low” frequency components of the reference data. The “high” frequency fit is a 20 point average along the reference curve. This fit exhibits similar features to the oscillatory noise present in the experimental data. The “low” frequency fit is a 120 point average which corresponds to the wavelength dependence of the detector and transmitter. Each of these fits is used as a weighted function in the analysis routine used for processing of the experimental data.

Each of the regions of the NIR spectrum exhibits absorption by atmospheric species and contains varying amounts of background noise. Measurements of a water vapor absorption feature centered near 945 nm show fewer fluctuations from oscillatory and random noise. In this case, more weight is placed on a low frequency data processing of the reference applied to the measurement. Figure 5-2 shows eight consecutive 30 second raw measurements of the water vapor absorption feature overlaid to demonstrate the repeatability, and indicates the precision of the measurement. Each measurement exhibits a small offset from each other, which is partially removed by the analysis techniques mentioned previously. The low frequency reference fit is also overlaid to reveal its’ correlation with the measurements.

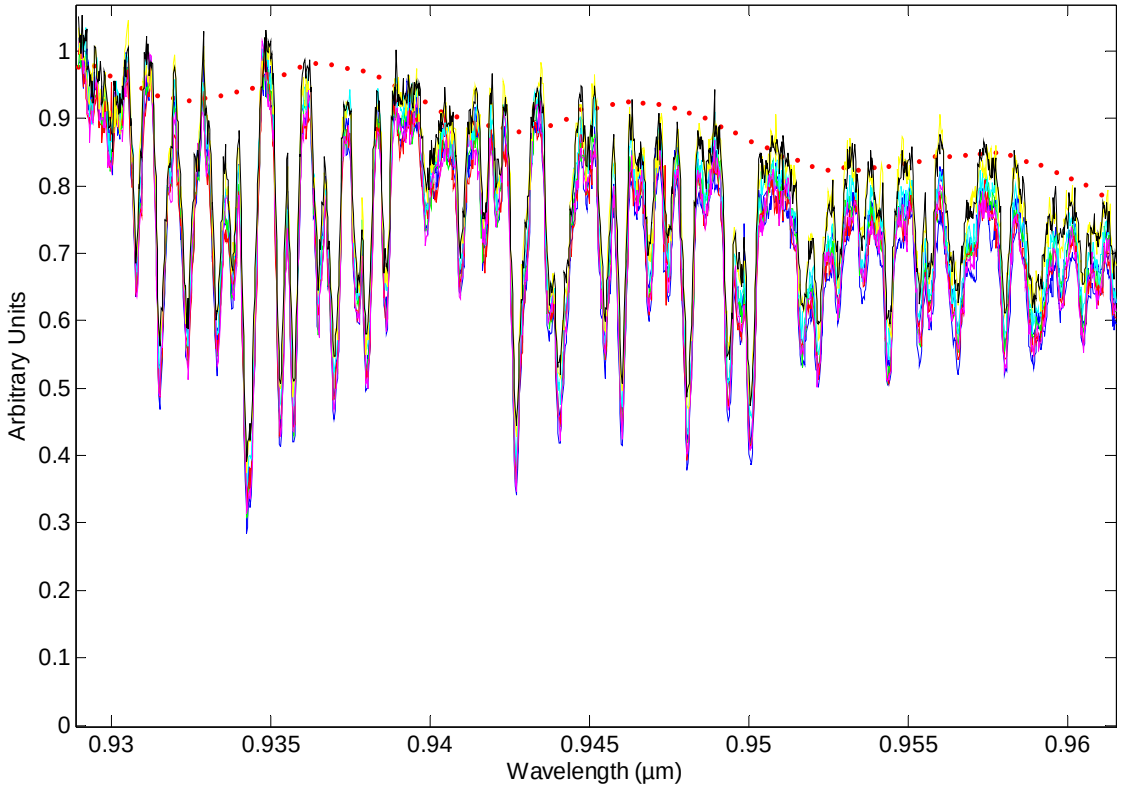


Figure **5-2**: Several water vapor absorption measurements superimposed demonstrating repeatability and the dotted line represents the reference spectrum fit used in the analysis procedure.

### 5.1.2 Multiwavelength Algorithm

The quantitative analysis technique for determination of species concentration is adapted from previously reported work using a multiwavelength maximum likelihood estimation (MLE) algorithm to calculate the CPL [Brown *et al.*, 2008b]. The techniques are modified here and applied to the long path measurements to determine the water vapor and oxygen concentrations presented in the subsequent sections. The application

of the algorithm to these long path lengths demonstrates its usefulness and extends the previous measurements from shorter path lengths.

The MLE algorithm adapts techniques developed by Warren [1996] and Yin and Wang [2006] for simultaneously analyzing several DIAL wavelength pairs, and it applies those ideas to a multiwavelength configuration that is capable of simultaneously analyzing hundreds of wavelength pairs. In a perfect world, the spectral dependence of each species present allows easy separation of the absorptivity and path integrated concentration, since they exist as elements in the standard lidar equation. Therefore, we calculate species concentration and absorptivity in parallel, and determine the concentration results through recursive iterations. The recursive algorithm for CPL is given from Brown [2008] as,

$$CPL_l = \frac{1}{n-1}\sum_{M=n-x}^{n}\left\{\frac{\sum_{j=1}^{M}\left[\alpha_{jl}\hat{\Lambda}_1^{-1}(j,j)\left[\hat{H}_1 - \overline{Q}(j) - \sum_{l=1,l\neq 1}^{L}\alpha_{jl}CPL_l\right]\right]}{\sum_{j=1}^{M}\left[\alpha_{jl}\hat{\Lambda}_1^{-1}(j,j)\alpha_{jl}\right]}\right\}\left[ppm\cdot m\right] \quad [5.1]$$

where,

$\hat{\Lambda}_1^{-1}$ is the noise covariance matrix,

$\hat{H}_1$ is the simulated signal,

$\alpha_{jl}$ is the specific absorption parameter, and

$\overline{Q}(j)$ are the integrated measurements.

For discussion of the main components of the inversion process, the reader is referred to the doctoral dissertation of Brown [2008].

## 5.2 Measurements and Calculations for Species Concentrations

Measurements for water vapor and atmospheric oxygen are presented in this section as examples of the sensor capability and to indicate the possibility of extending to other species measurements. These atmospheric constituents are the primary absorbing species at wavelengths within the bandwidth of the supercontinuum laser source used for these investigations. A MODTRAN™ 5 simulation for the horizontal transmittance through the atmosphere for an 890 m path is shown in Figure 5-3. The figure shows the spectral features of several water vapor and oxygen bands as well as two minor constituents, methane and carbon dioxide, in the spectral region that can possibly be measured with current hardware. The techniques for analysis described in section 5.1,

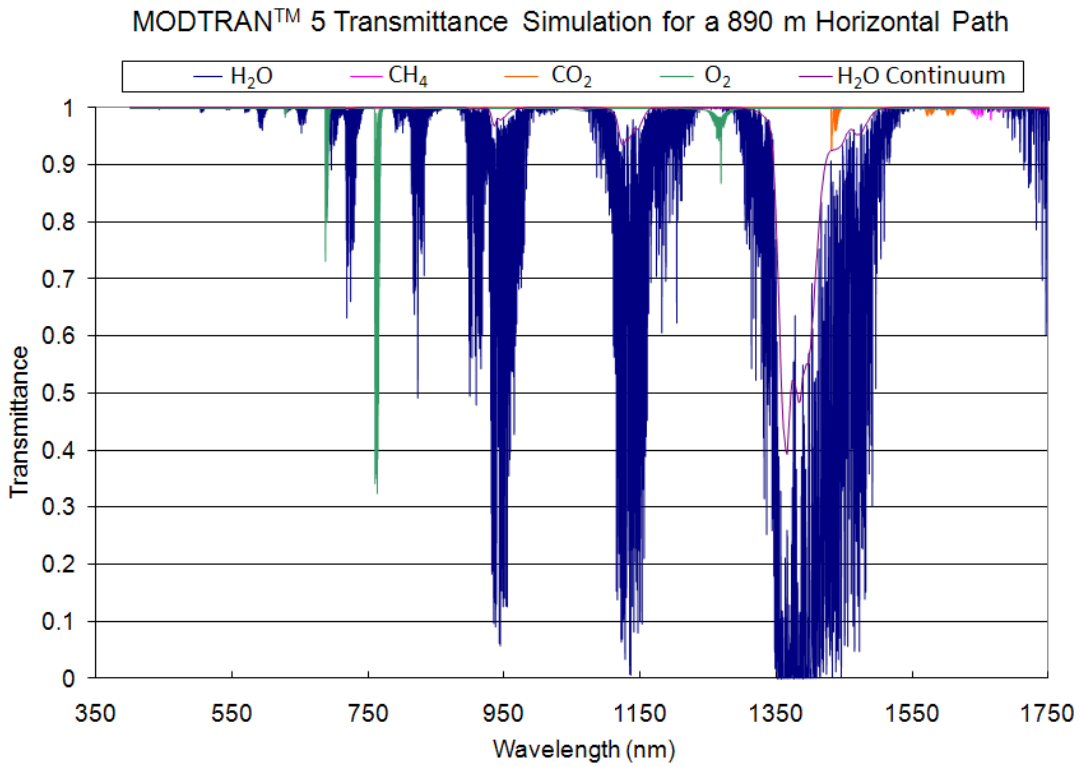


Figure **5-3**: MODTRAN™ 5 transmittance simulation for the atmospheric constituents present within the spectral bandwidth of the supercontinuum source.

are implemented for integrated path concentration values of the species, and to demonstrate the high-quality of comparisons with simulated spectra.

### 5.2.1 Long Path Water Vapor Measurement

The laboratory measurements for water vapor concentration in air, reported by Begnoché [2005], were the first demonstrations of the Penn State SAS approach to measure gaseous species concentrations. Later, open path atmospheric measurements for water vapor content were demonstrated by Brown *et al.* [2008a and 2008b], extending the capability for measurements to 150 and 300 m path lengths. These measurements focused on obtaining NIR spectra of the water vapor absorption feature centered at 1400 nm, and correlated very well with simulated transmittance data. Additionally, inversion estimates for relative humidity were accurate to within a few percent of a set of nearby MET station point measurements. These previous measurements demonstrated that accurate water vapor results are obtained on relatively short atmospheric path lengths.

However, over longer path lengths, the 1400 nm water vapor absorption band begins to saturate (see Figure 4-3), making accurate measurements difficult at those wavelengths. Brown [2008] encountered similar issues while transferring from short laboratory path measurements to outdoor measurements. Fortunately, water vapor can be measured over longer path lengths, using one of the several other water vapor bands associated with overtones of the water spectrum that are located at shorter wavelengths in the NIR. Less absorption occurs in bands centered at 1140 and 945 nm; while even lower absorption occurs at bands centered at 840 and 730 nm. The logical choice in our case

for remote sensing on paths that are saturated in the 1400 nm range is to use the absorbing band centered at 1140 nm, and it should present better signals to determine the concentration. However, the supercontinuum laser pump at 1064 nm generates significant structure and non-uniformity in the spectra near the pump wavelength range. Several trials showed that the 945 nm wavelength band is a better choice for accurate sensing, and produces better results than the 1140 nm region.

Measurements for water vapor absorption over the 890 m path acquired during the early morning hours of March 6, 2009 are shown in Figure 5-4. The spectral measurements are analyzed using the techniques previously described in section 5.1. A measurement is superimposed on the MODTRAN$^{TM}$ calculation for the conditions of this measurement. The spectral features in a 30 nm region centered at 945 nm agree well with the corresponding simulation, when spectral alignment and peak (valley) locations are compared; however, differences in the relative absorption strengths of the lines are significant. There are several factors contributing to this result. MODTRAN$^{TM}$ is not adjusted for the meteorology present during the time of measurement. Instead, the simulation implemented relies on model and seasonal predications for the transmittance calculations. A more comprehensive realization of MODTRAN$^{TM}$ is required for this comparison. Thus, in the case of this comparison, absorption levels are expected to differ in the water vapor measurements as increased or decreased relative humidity values over seasonal averages will modify the absorption present at the time of measurement.

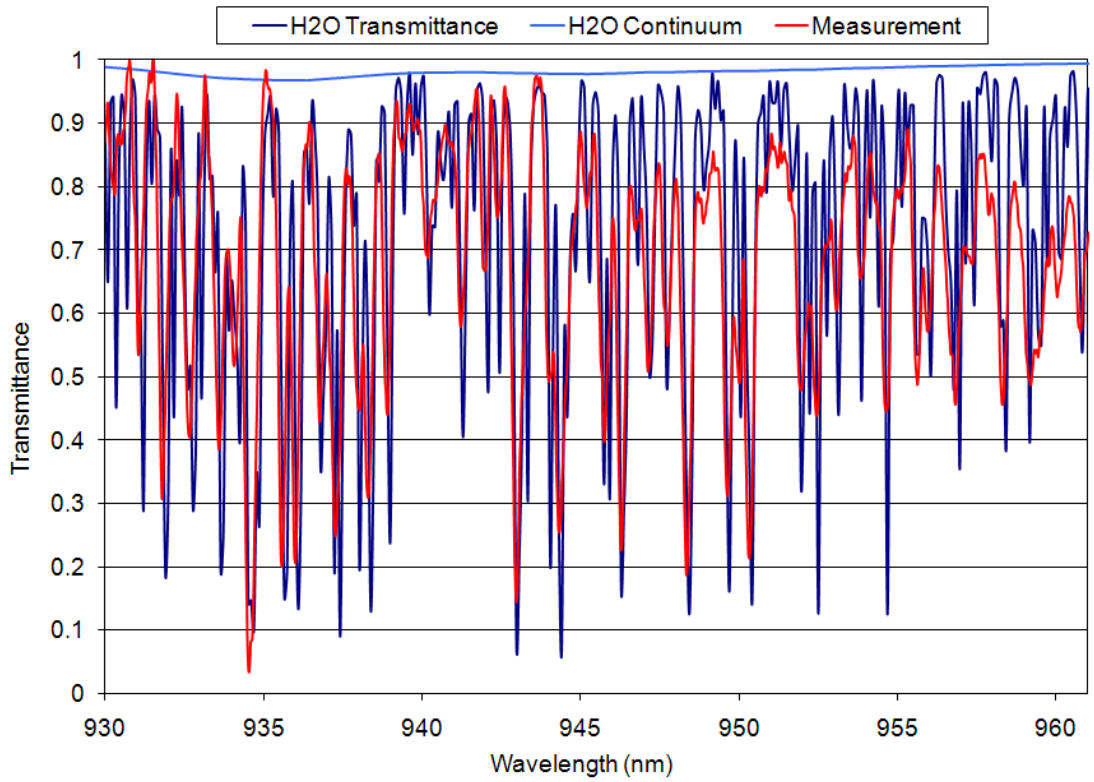


Figure **5-4**: The measured absorption spectra for atmospheric water vapor transmittance at 1 $cm^{-1}$ resolution over the 890 m path are compared with a MODTRAN$^{TM}$ 5 simulation.

The measurement is again shown in Figure 5-5 (a) and compared with HITRAN cross sections broadened for temperature and pressure corresponding to the conditions at the time of measurement. The cross-section calculations are also convolved with a slit width function determined to optimize the correlation for comparison with the measured data. A slit width value of 6.42 $cm^{-1}$ was found in earlier experiments by Brown *et al.* [2008b] as the optimum value for the inversion algorithm performance during analysis for a previous SAS configuration, and the same value also provides the highest correlation between the calculation and the smoothed measurement in this case.

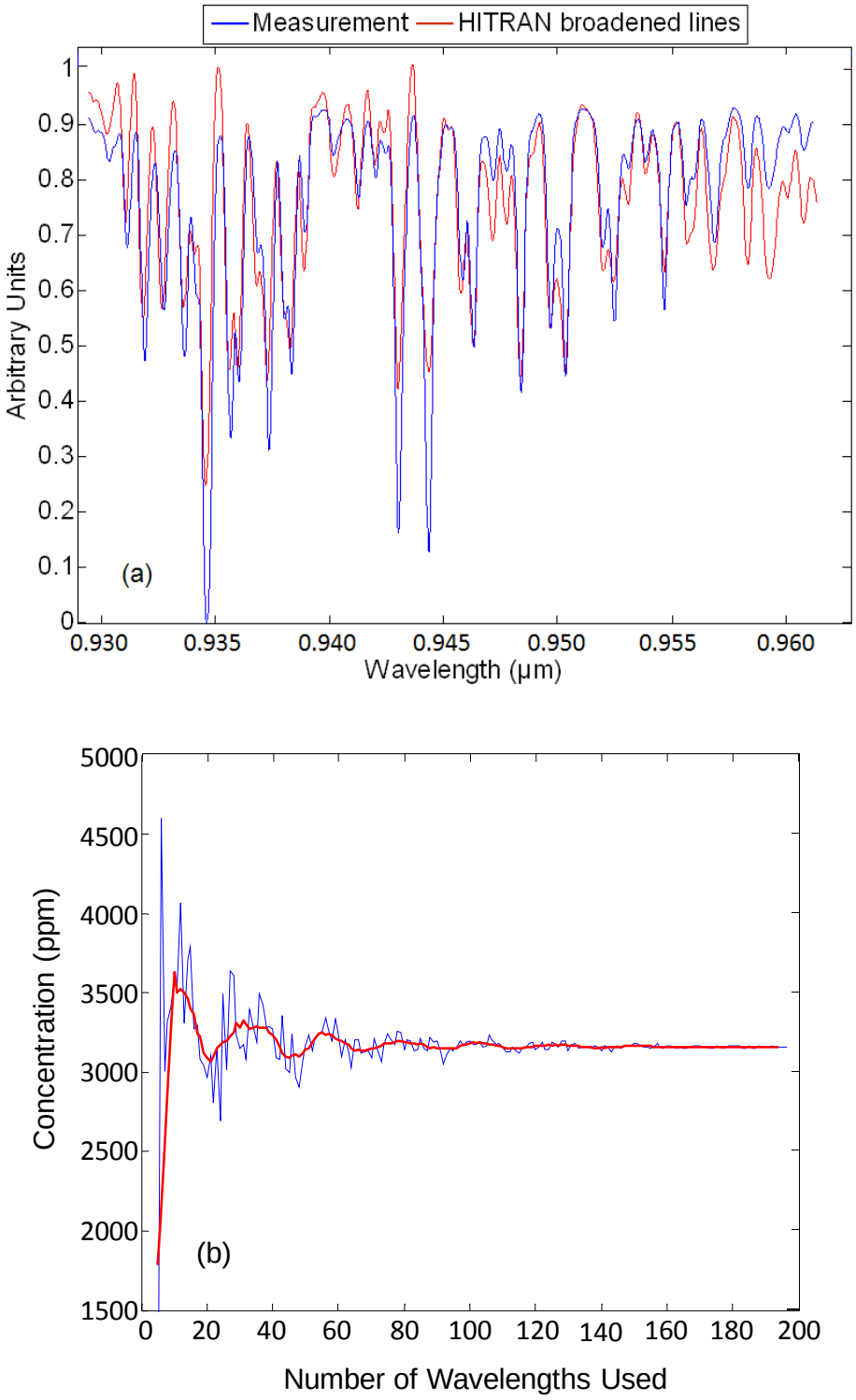


Figure **5-5**: (a) HITRAN line calculations broadened for temperature and pressure are convolved with the slit width of 6.4 $cm^{-1}$ to compare to the high resolution measurement from Figure 5-4. (b) MLE algorithm inversion result for estimation of water vapor concentration.

The results from applying of the MLE algorithm are shown in Figure 5-5 (b). The algorithm demonstrates good convergence to a concentration value of 3161 ± 7.3 ppm long before the 200 wavelengths in the inversion calculation plotted. A local meteorological station recorded temperature and relative humidity throughout the night of measurement and these recordings are shown in Figure 5-6. At the time of SAS measurements of water vapor absorption, the temperature was recorded as 6°C and relative humidity as 40%. A conversion formula reported by Lowe [1977] is used for calculation of water vapor concentration given relative humidity and temperature. The

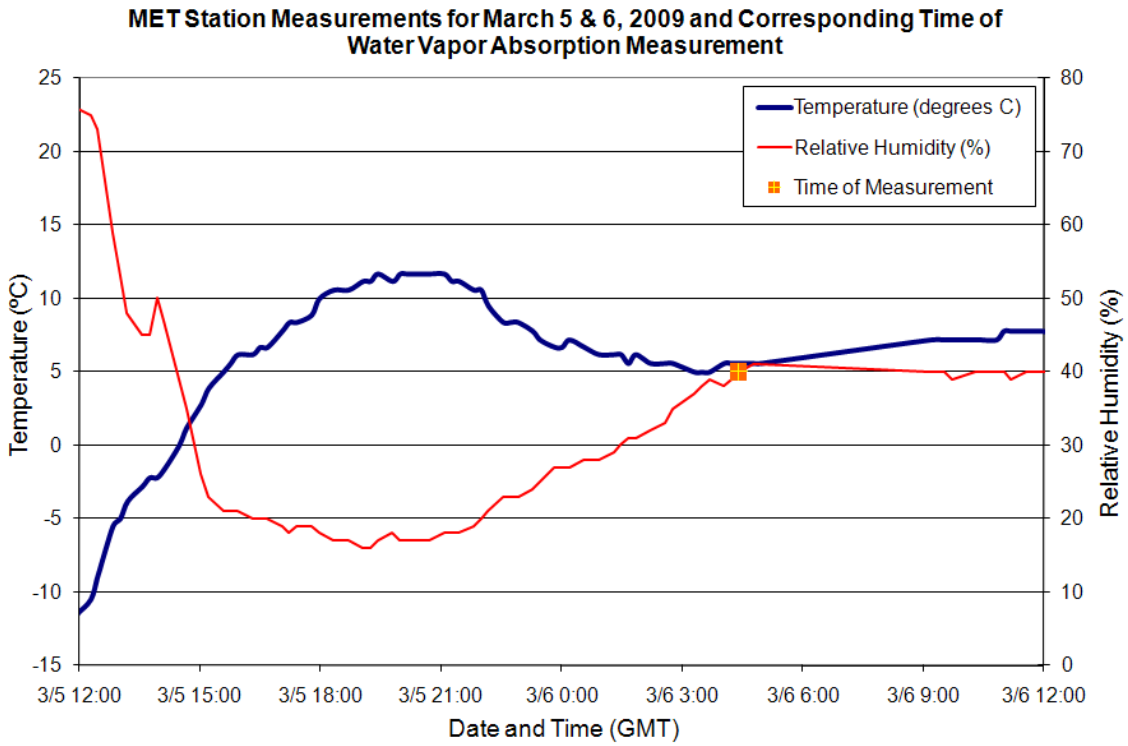


Figure **5-6**: Measurements of relative humidity and temperature recorded a MET station located 5 m from the measured path at the time of SAS water vapor measurements indicated.

calculated value of 3027.7 ppm is 4.2% lower than the path measured value. Differences are expected as variances in humidity become more prominent across longer path lengths. However, this measurement shows the same order of magnitude as the atmospheric differences found previously for shorter path lengths [Brown *et al.*, 2008a].

### 5.2.2 Long Path Oxygen Measurement

The NIR spectral region between 740 and 780 nm is useful for studies of small oxygen variations in the atmosphere. Within this region there exist several strong oxygen absorption features and only a few interfering species, such as the water vapor absorption. Therefore, acquisition of broadband spectra in this region permits analysis of the concentration-path-length (CPL) value of oxygen using the previously described MLE inversion. Figure 5-7 shows measured absorption spectra captured by a high resolution CCD spectrometer configured for an effective resolution of 1.43 $cm^{-1}$. Comparisons to a MODTRAN™ 5 simulation are made by adjusting the simulation to shift from the vacuum to air index of refraction, for the temperature and pressure recorded during measurement. A curve representing a fifteen measurement average with the calculated standard deviation of ±0.0117 is also overlaid in Figure 5-7 to demonstrate consistency of the measurements. The data was recorded during a 10 minute interval and the mechanical mode-filtering techniques, described in Chapter 4, were applied to the fibers from the laser source and to the roof-top transceiver configuration back to the spectrometer. The measurements and simulation show good correlation across several of the "double-peaked" sections of the absorption feature, as well as within the group of

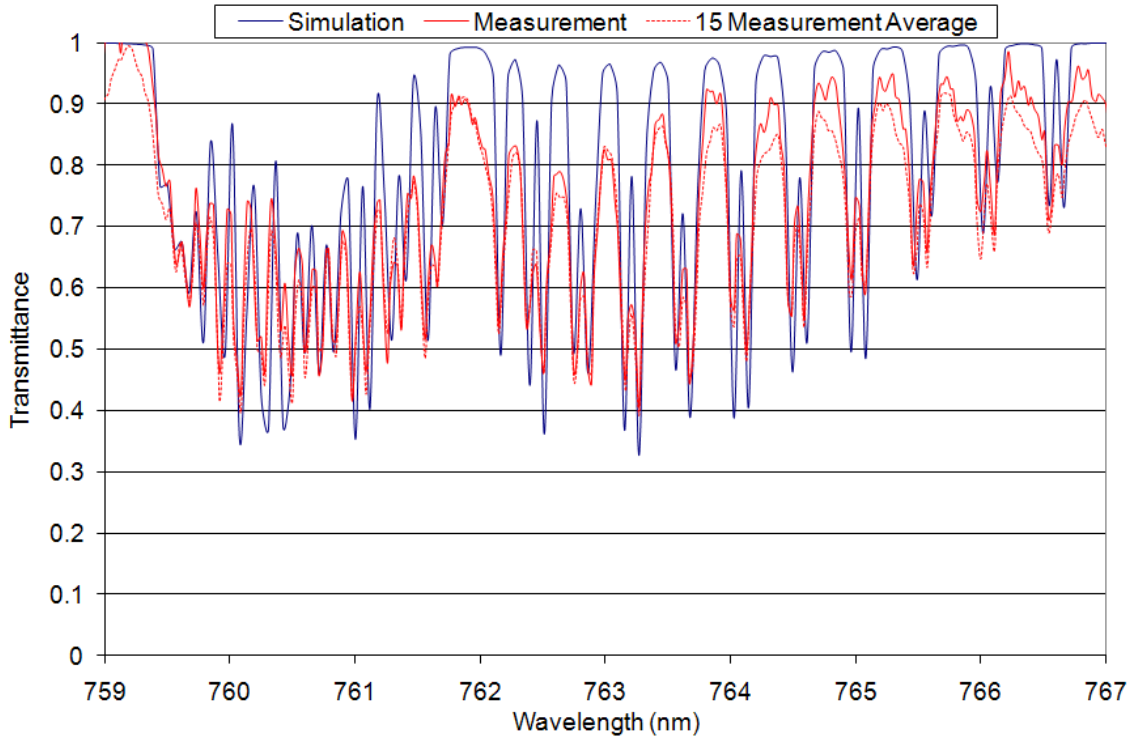


Figure 5-7: MODTRAN™ 5 Simulated transmittance spectra showing an oxygen absorption band and a long path absorption measurement for the same region superimposed for comparison.

lines near 760.5 nm. The differences between several of the peak values compared to simulation, are generally attributed to signal noise introduced by optical mode interference in the fiber coupling.

Figure 5-8(a) shows the measured absorption spectra prepared for processing through the MLE inversion algorithm. The measured spectra are convolved with a 6.4 $cm^{-1}$ slit width Gaussian window to smooth the data for better convergence from the MLE. The same window is used to calculate the linewidth for the high resolution HITRAN oxygen lines and applied in the calculation of the CPL. The convergence of the MLE inversion is depicted in Figure 5-8(b). The calculated concentration resulting from the analysis of the measured absorption of atmospheric oxygen lines in the 890 m path is

208640 ± 63 ppm. This 20.86% value is about 0.09% lower than the nominally accepted mixing ratio for dry atmospheric oxygen which is 20.95%. The quick convergence of the inversion algorithm and its' precision suggests that error in this calculation is most likely attributed to path length measurement discrepancies. Approximately 4 m less in path distance would account for the difference in the calculated concentration.

Another measurement for atmospheric oxygen was acquired on the same night as the water vapor measurement presented in the previous section. The measurement used the spectrometer slit width set to 250 μm, and corresponds to an effective slit width of 7.15 $cm^{-1}$. This measurement is acquired at a significantly lower resolution than the previous one. The HITRAN lines used in the MLE inversion were convolved with the 7.15 $cm^{-1}$ slit width and the inversion calculation of the concentration is shown in Figure 5-9. This inversion required 100 wavelengths versus the 200 used in the previous analysis. The concentration calculation results from a 20 point average and is 211400 ± 119 ppm (21.14%), or 0.19% higher than the accepted dry atmosphere value.

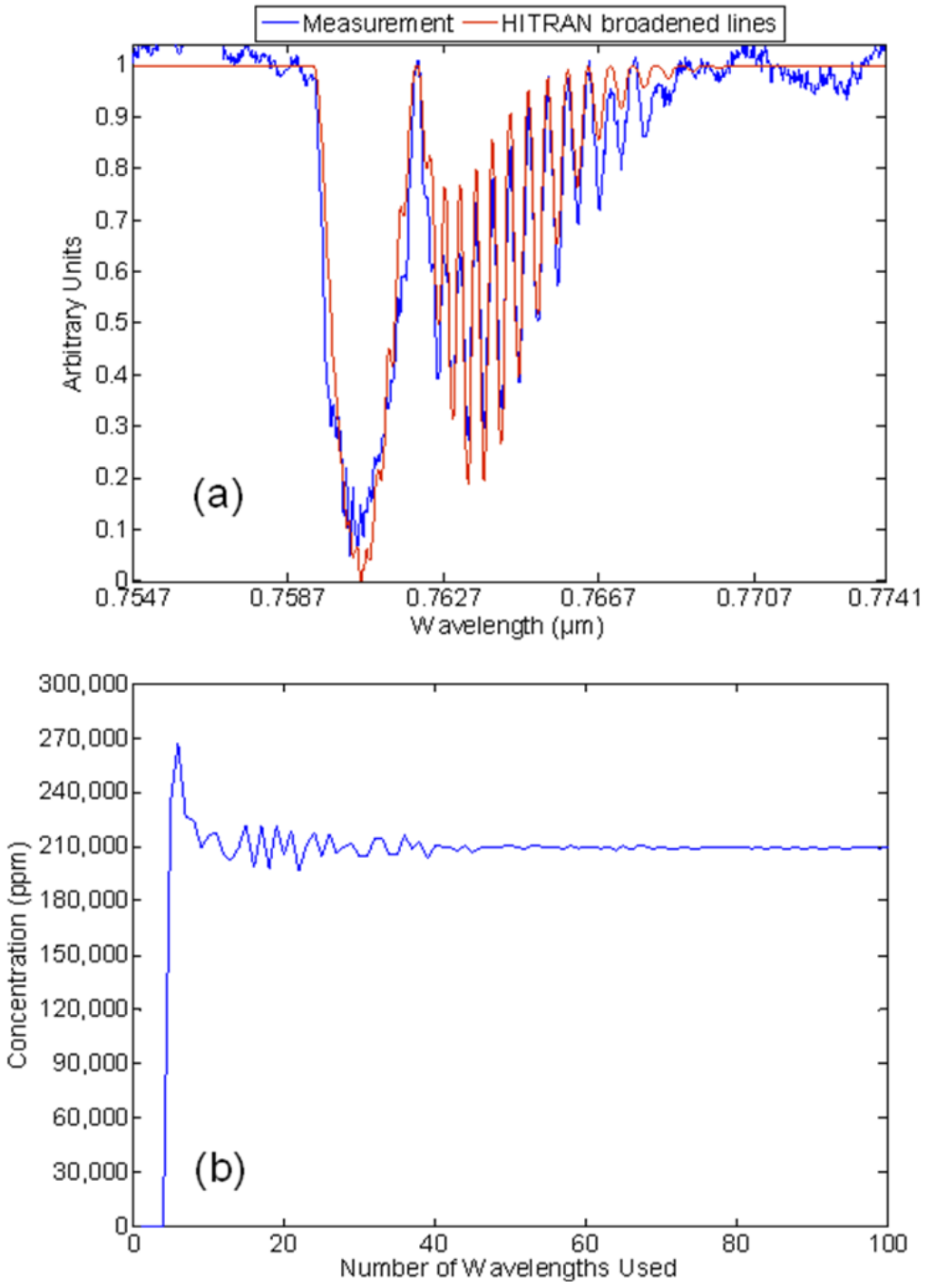


Figure **5-8**: (a) HITRAN line calculations (blue line) broadened for temperature and pressure, then convolved with the slit width of 6.4 $cm^{-1}$ compared with the high resolution measurement for oxygen shown in Figure 5-7 (red line). (b) MLE inversion algorithm result for atmospheric oxygen demonstrating quick convergence on the concentration value.

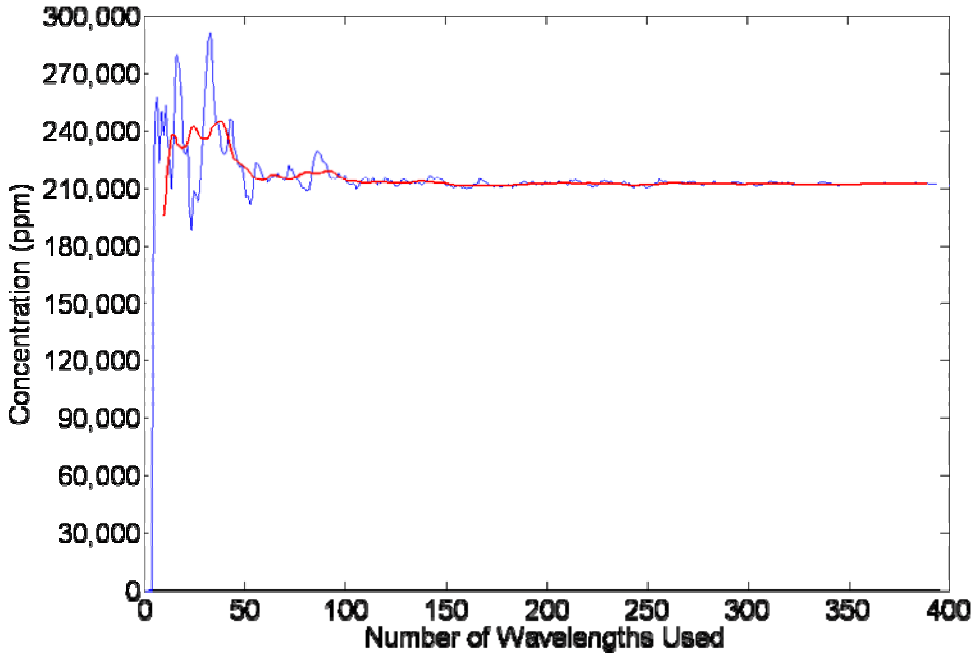


Figure **5-9**: MLE algorithm inversion convergence calculation for atmospheric oxygen using 400 wavelengths in the 750 to 775 nm region. A 20 point average of the resulting is also shown (red line).

## 5.3 Summary

The supercontinuum absorption measurements presented in this chapter are found to correlate well with MODTRAN$^{TM}$ and HITRAN simulations of the spectra. Integrated path length concentration values for the water vapor measurements agree with the MET station point measurements, and the measurements for oxygen concentrations are calculated within 0.1% of the accepted atmospheric oxygen mean concentration. The analysis techniques described provide a suitable method for preparing the data for comparison with simulated spectra, and the MLE algorithm used for determination of species concentration is tested and is acceptable for the path length of 890 m.

# Chapter 6

# Summary, Conclusions and Future Work

## 6.1 Summary

The primary goals for this research are to extend SAS to measure atmospheric species concentrations on a long path and to maintain or improve measurement accuracy compared to previous species measurements along shorter paths [Brown *et al.*, 2008a and 2008b]. Long path supercontinuum laser returns were measured by a grating spectrometer which generated spectral data. The spectral regions examined demonstrate the capability to measure oxygen and water vapor absorption over a 1 km path length and process spectral data using a multiple-line differential absorption MLE inversion algorithm. Spectral data from 750 to 775 nm was input to the algorithm and converged on a CPL of 208640 ± 63 ppm and within 0.1% of the mean dry atmosphere value of 20.95% for oxygen. The spectral region of 930 to 960 nm was analyzed for water vapor absorption and the inversion algorithm converged on a CPL of 3161 ± 7.3 ppm. This result for water vapor concentration is 4.2% larger than measurements from a nearby MET station. The accuracy of the SAS measurements demonstrates that the current system is quite capable of NIR measurements of atmospheric species on path lengths of 1 km range.

## 6.2 Conclusions

Supercontinuum absorption spectroscopy combines many of the best aspects of DIAL, DOAS, and hyperspectral measurement techniques to achieve measurements of species concentrations with small error in the presence of a mixture of other species. A spectrally broad supercontinuum laser source is used for multiwavelength analysis of the differential absorption measured across several hundred wavelength pairs to detect and measure the concentration of atmospheric species with improved accuracy, specificity, and discrimination against interfering species in the spectral region.

Broadband spectral measurements of atmospheric water vapor and oxygen are presented as a demonstration of the capability of the SAS technique, and their concentrations are calculated using a multiwavelength inversion algorithm. The sensitivity of these measurements was influenced, and in some cases limited, by the necessary experimental arrangement of components used in the SAS system. The two key elements of the primary system limiting the accuracy of these experiments are caused by the supercontinuum laser source and the long fibers coupling the source and detector. While the laser's broadband stability is generally maintained during operation, narrowband portions of the laser spectrum exhibited small scale noise fluctuations. This is due to the spectral stability and sensitivity to variations in pump power, temperature, coupling efficiency into the nonlinear fiber, and interference of higher order modes in the long fibers used to couple the components of the experiment. The measurements presented in this work examine this added noise in portions of the spectra where low absorption measurements were studied. This noise was coupled together with high order,

high frequency modal noise produced in the long length fibers, as discussed in Chapter 4. These sources of noise are the primary contributors to limiting the precision of the SAS system and require improvement in future implementations of the supercontinuum absorption spectroscopy approach to atmospheric sensing.

## 6.3 Future Work

The SAS measurements and capability demonstrated in this work, expand upon the previous research by Begnoché [2005], and Brown [2008]. This research serves as proof of the ability to extend the technique from short to long range detection of atmospheric species, using a laboratory configuration of components for a supercontinuum laser system. In recent years, improvements in fiber laser technology and supercontinuum stability have sparked the emergence of several turn-key laser systems capable of higher power, broader spectral range supercontinuum generation. Future investigations of SAS will seek to use these types of sources for enhanced detection of NIR absorbing species including carbon dioxide and methane, as well as investigations of many trace species that can be studied when the technique is extended to longer wavelengths.

Mid-wave infrared (MWIR) supercontinuum absorption spectroscopy of atmospheric species is also a primary future goal. Brown [2008] developed several techniques for MWIR detection of hydrocarbons in the 3 to 5 micron region and also indicated the future application of MWIR SAS sensing. Development of a supercontinuum source capable of MWIR generation is needed to extend the wavelength

range of the current supercontinuum sources, which have been limited by the properties of materials that prevents supercontinuum generation at longer wavelengths. However, supercontinuum generation from 0.8 to 4.5 μm was demonstrated successfully by Xia *et al.* [2006] in ZBLAN fluoride fibers indicating the potential for this technology. Further study and development of MWIR supercontinuum will greatly extend the capability and value of SAS atmospheric sensing measurements.

**References**

Alfano, R.R. 1989. *Supercontinuum Laser Source*, 2nd edn, Springer, New York, NY.

Atkins, P.W. 1990. *Physical Chemistry*, 4th edn, W.H. Freeman and Company, New York, NY.

Begnoché, J. 2005. *Analytical Techniques for Laser Remote Sensing with a Supercontinuum White Light Laser*, Master's Thesis, The Pennsylvania State University, University Park, viewed July, 2009, <http://lidar1.ee.psu.edu/thesissite_eee.htm>.

Berk, A., Cooley, T.W., Anderson, G.P., Acharya, P.K., Bernstein, L.S., Muratov, L., Lee, J., Fox, M.J., Adler-Golden, S.M., Chetwynd, J.H., Hoke, M.L., Lockwood, R.B., Gardner, J.A. and Lewis, P.E. 2004. "MODTRAN5: A reformulated atmospheric band model with auxiliary species and practical multiple scattering options," *Proc. of the SPIE Algorithms and Technologies for Multispectral, Hyperspectral, and Ultraspectral Imagery XI*,, vol. 425, pp. 341-347.

Berk, A., Bernsten, L.S., and Robertson, D.C. 1989. *MODTRAN$^{TM}$: A Moderate Resolution Model for LOWTRAN7.* Air Force Geophysics Laboratory, Hanscom AFB, MA, GL-TR-89-0122, pp. 38.

Brown, D.M. 2008. *Multi-wavelength Differential Absorption Measurements of Chemical Species*, Ph.D. Dissertation, The Pennsylvania State University, University Park, viewed January 2009, <http://lidar1.ee.psu.edu/thesissite_eee.htm>.

Brown, D.M., Shi, K., Liu, Z. and Philbrick, C.R. 2008a. "Long-path supercontinuum absorption spectroscopy for measurement of atmospheric constituents," *Optics Express*, vol. 16, pp. 8457-8471.

Brown, D.M., Liu, Z. and Philbrick, C.R. 2008b. "Supercontinuum lidar applications for measurements of atmospheric constituents," *Proc. of the SPIE Laser Radar Technology and Applications XII*, vol. 6950, pp. 69500B-69500B-11.

Edwards, P.S., Wyant, A.M., Brown, D.M., Liu, Z., Philbrick, C.R. 2009, "Supercontinuum Laser Sensing of Atmospheric Constituents" *Proc. of the SPIE Laser Radar Technology and Applications XIV*, Vol. 7323, 73230S-73230S-8.

Geyer, A., Alicke, B., Konrad, S., Schmitz, T., Stutz, J., Platt, U. 2001. "Chemistry and oxidation capacity of the nitrate radical in the continental boundary layer near Berlin," *J. Geophys. Res*, vol. 106, pp. 8013–8025.

Heaps, W.S. 2008. "Broadband Lidar technique for precision CO2 measurement," *Proc. of the SPIE Lidar Technologies, Techniques, and Measurements for Atmospheric Remote Sensing IV*, vol. 7111, pp. 711102-711102-9.

IPCC-AR4, 2007. Forster, P., V. Ramaswamy, P. Artaxo, T. Berntsen, R. Betts, D.W. Fahey, J. Haywood, J. Lean, D.C. Lowe, G. Myhre, J. Nganga, R. Prinn, G. Raga, M. Schulz and R. Van Dorland, 2007: Changes in Atmospheric Constituents and in Radiative Forcing. In: Climate Change 2007: The Physical Science Basis. Contribution of Working Group I to the Fourth Assessment Report of the Intergovernmental Panel on Climate Change [Solomon, S., D. Qin, M. Manning, Z. Chen, M. Marquis, K.B. Averyt, M.Tignor and H.L. Miller (eds.)]. Cambridge University Press, Cambridge, United Kingdom and New York, NY, USA.

Lowe, P.R. 1977. “An approximating polynomial for the computation of saturation vapor pressure,” *Journal of Applied Meteorology*, vol. 16, pp. 100-102.

Measures, R.M. 1984, *Laser Remote Sensing*,Wiley-Interscience, New York, NY.

Mie, G. 1908. “Beitraege zur Opitek trueber Medien, speziell kolloidaler Metalosungen,” *Ann. Phys.*, vol.25, pp. 377-445.

Murdock, D.G., Stearns, S.V., Lines, R.T., Lenz, D., Brown, D.M. and Philbrick, C.R. 2008. “Applications of real-world gas detection: Airborne Natural Gas Emission Lidar (ANGEL) system,” *J. Appl. Remote Sens.*, vol. 2, pp. 1-18.

NOAA/ESRL, 2009. NOAA Earth System Research Laboratory: Global Monitoring Division, accessed May, 2009 <http://www.esrl.noaa.gov/gmd/dv/ftpdata.html>.

Philbrick, C. R., Brown, D.M., Willitsford, A.H., Edwards, P.S., Wyant A.M., Liu, Z., Chadwick, C.T., Hallen, H. 2009. “Remote Sensing of Chemical Species in the Atmosphere,” *Proc. of Fourth Symposium on Lidar Atmospheric Applications* 1.1, 89th AMS Annual Meeting, Phoenix, AZ.

Platt, U. 2004. “Differential optical absorption spectroscopy (DOAS)” in *Air Monitoring by Spectroscopic Techniques*, M.W. Sigrist, ed., John Wiley and Sons, pp. 27-84.

Platt, U., Stutz, J., 2008. *Differential Optical Absorption Spectroscopy: Principles and Applications*, Springer-Verlag, Berlin.

Schotland, R. M. 1965. "The Determination of the Vertical Profile of Atmospheric Gases by Means of a Ground Based Optical Radar," *in Proceedings of the Third Symposium on Remote Sensing of Environment, October 1964* (U. Michigan, Ann Arbor,).

Stothard, D.J.M., Dunn, M.H. and Rae, C.F. 2004. “Hyperspectral imaging of gases with a continuous-wave pump-enhanced optical parametric oscillator” *Optics Express*, vol. 12, pp. 947-953.

Stutz, J., Alicke, B., Ackermann, R., Geyer, A., White, A., Williams, E. 2004. “Vertical profiles of NO3, N2O5, O3, and NOX in the nocturnal boundary layer: 1. Observations during the Texas Air Quality Study 2000,” *J. Geophys. Res.*, vol. 109, pp. D12306. doi:10.1029/2003JD004209

USSA76, U.S. Committee on Extension to the Standard Atmosphere (COESA), *U.S. Standard Atmosphere, 1976*, U.S. Government Printing Office, Washington, D.C.

Wadsworth, W., Joly N., Knight J., Birks T., Biancalana F., and Russell P. 2004, "Supercontinuum and four-wave mixing with Q-switched pulses in endlessly single-mode photonic crystal fibres," Opt. Express 12, 299-309.

Warren, R.E. 1996. “Optimum detection of multiple vapor materials with frequency-agile lidar,” *Appl. Opt*., vol. 35, pp. 4180-4193.

Wyant, A. M., Brown, D.M., Edwards, P.S., Philbrick, C.R. 2009, “Multi-wavelength, multi-angular lidar for aerosol characterization” *Proc. of the SPIE Laser Radar Technology and Applications XIV*, Vol. 7323, 73230R-73230R-8.

Xia, C., Kumar, M., Kulkarni, O.P., Islam, M.N., Terry, F.L., Freeman, M.J., Poulain, M. and Maze, G. 2006. “Mid-infrared supercontinuum generation to 4.5 μm in ZBLAN fluoride fibers by nanosecond diode pumping,” *Opt. Letters*, vol. 31, pp. 2553-2555.

Yin S. and Wang, W. 2006. “Novel algorithm for simultaneously detecting multiple vapor materials with multiple-wavelength differential absorption lidar,” *Chin. Opt. Lett*., vol. 4, pp. 360-362.

Young, A. T. 1981. "Rayleigh scattering," *Appl. Opt.*, vol. 20, pp. 533-535.